

Measuring Star Formation Histories from Asymptotic Giant Branch Stars: A Demonstration in M31

ABIGAIL J. LEE,^{1,2} DANIEL R. WEISZ,³ YI REN,⁴ ALESSANDRO SAVINO,³ AND ANDREW E. DOLPHIN^{5,6}

¹*Department of Astronomy & Astrophysics, University of Chicago, 5640 South Ellis Avenue, Chicago, IL 60637*

²*Kavli Institute for Cosmological Physics, University of Chicago, 5640 South Ellis Avenue, Chicago, IL 60637*

³*Department of Astronomy, University of California, Berkeley, CA 94720-3411, USA*

⁴*College of Physics and Electronic Engineering, Qilu Normal University, Jinan 250200, China*

⁵*Raytheon Technologies, 1151 E. Hermans Road, Tucson, AZ 85756, USA*

⁶*Steward Observatory, University of Arizona, 933 N. Cherry Avenue, Tucson, AZ 85719, USA*

ABSTRACT

We demonstrate how near infrared (NIR) imaging of resolved luminous asymptotic giant branch (AGB) stars can be used to measure well-constrained star formation histories (SFHs) across cosmic time. Using UKIRT *J* and *K*-band imaging of M31, we first show excellent agreement over the past ~ 8 Gyr between the PHAT SFH of M31’s outer disk derived from a deep optical color-magnitude diagram (CMD; $\sim 3.3 \times 10^7$ stars with $M_{F814W} \lesssim +2$), and our spatially-matched SFH based only on modeling AGB stars on a NIR CMD ($\sim 2.3 \times 10^4$ stars with $M_J \lesssim -5$). We find that only hundreds of AGB stars are needed for reliable SFH recovery, owing to their excellent age sensitivity in the NIR. We then measure the spatially resolved SFH of M31’s inner stellar halo ($D_{\text{M31,projected}} \sim 20 - 30$ kpc) using $\sim 10^5$ AGB stars. We find: (i) a dominant burst of star formation across M31’s inner stellar halo from 4 – 5 Gyr ago and lower level, spatially distributed star formation $\sim 1 - 2$ Gyr ago; (ii) a younger ‘quenching time’ in the vicinity of NGC 205 (~ 1 Gyr ago) than near M32 (~ 1.1 Gyr ago); (iii) $M_\star \sim 4 \pm 0.5 \times 10^9 M_\odot$ formed over the past ~ 8 Gyr. We discuss some caveats and the enormous potential of resolved AGB stars in the NIR for measuring SFHs back to ancient epochs (~ 13 Gyr ago) in galaxies to large distances ($D \gtrsim 20$ Mpc) with JWST, Roman, and Euclid.

Keywords: Andromeda Galaxy (39), Asymptotic giant branch (108), Galaxy stellar halos (598), Near infrared astronomy (1093), Stellar populations (1622), Asymptotic giant branch stars (2100)

1. INTRODUCTION

Asymptotic giant branch (AGB) stars represent the final nuclear-fusing evolutionary phase for low and intermediate-mass ($0.5 - 8 M_\odot$), intermediate-age (~ 100 Myr to ~ 14 Gyr ago) stars. With peak spectral energy distributions at $\sim 1.5 \mu\text{m}$, they are among the brightest stars in the near-infrared (NIR; Maraston et al. 2006; Melbourne et al. 2012; Melbourne & Boyer 2013, and are known to exist in abundance in a wide variety of galaxies from low-metallicity dwarf galaxies to high-metallicity massive ellipticals (e.g., Gallart et al. 1996; Dalcanton et al. 2012a; Rejkuba et al. 2022; Anand et al. 2024a,b; Hoyt et al. 2024; Lee et al. 2024). Further-

more, there exists a clear mapping between some of their observable properties (i.e., NIR colors and luminosities) and their ages (e.g., Gallart et al. 2005).

However, despite being ubiquitous, observational challenges and the physical complexity of AGB star physics have resulted in them playing a limited role in star formation history (SFH) measurements from optical resolved star color-magnitude diagrams (CMDs) in favor of better understood phases of evolution (e.g., main sequence turnoff, sub-giant branch, red clump; Gallart et al. 2005). In terms of observations, in the optical it is challenging to cleanly differentiate between AGB and red giant branch (RGB) stars, which are far less sensitive to age, as RGB stars with different ages can occupy similar regions of the CMD. From a physics standpoint, accurately modeling the color and magnitudes of AGB stars on a galaxy’s CMD requires a detailed under-

standing of complex processes in the interiors and atmospheres of AGB stars such as convection, overshooting, hot bottom burning, mass loss, dredge up, and pulsation (Gallart et al. 2005; Marigo et al. 2017; Pastorelli et al. 2019, 2020). The comparatively simple physics for other age-sensitive populations (MSTO, SGB, RC) has made them the staple of accurate SFH modeling despite their less favorable observational properties, such as faintness and increased susceptibility to crowding (e.g., Gallart et al. 2005).

Nevertheless, a handful of pioneering studies recognized the potential of AGB stars for age determinations. Gallart et al. (1996) was the first to suggest AGB stars as a means of measuring a SFH through CMD modeling, noting: “...the potential power of AGBs as tracers of the SFH at intermediate ages (1–10 Gyrs). It can be reasonably be expected that, in the near future when uncertainties in the stellar evolutionary models for AGBs have been overcome, AGBs will provide strong, detailed insight into the SFH for that time interval.” Since then, NIR observations of AGB stars have been used to map spatially resolved stellar ages in nearby galaxies (e.g., Frogel & Blanco 1983; Reid & Mould 1984; Wood et al. 1985; Costa & Frogel 1996; Davidge 2003, 2005; Cioni et al. 2006, 2008; Melbourne et al. 2010; Jung et al. 2012; Crnojević et al. 2013; Davidge 2014; McQuinn et al. 2017). However, many of these studies relied on fairly rudimentary AGB star models and, in many cases, undertook simplified statistical approaches that did not capture the full complexity of CMD modeling or only pursued qualitative analysis. For example, Javadi et al. (2011) began an ambitious observational campaign to measure the SFHs of nearby galaxies by comparing the J and K band luminosity functions of their AGB populations to isochrones to estimate their initial stellar masses, and therefore ages. For computational tractability, they adopted simplifying assumptions like a single metallicity and did not use artificial star tests (ASTs). This methodology has been extended to a number of subsequent studies that highlight the scientific power of AGB stars in the NIR (e.g., Rezaeikh et al. 2014; Hamedani Golshan et al. 2017).

A more recent approach has been to compute the ratio of AGB to RGB stars in optical imaging to estimate the quenching epoch (i.e., the age of the youngest stellar population) using theoretical models or empirical relations derived from the SFHs of Local Group (LG) galaxies with deep CMDs (e.g., Rejkuba et al. 2022; Harmsen et al. 2023). Its application to several nearby galaxies both showcases the broad strengths of AGB stars for measuring important star formation timescales in galax-

ies outside the LG, while also highlighting limitations of AGB stars on optical CMDs.

In this paper, we combine NIR imaging, significant improvements in theoretical AGB stars models, and well-established CMD fitting techniques to measure quantitative, ‘non-parametric’ SFHs using only AGB stars. The increase in high-quality NIR resolved star photometry, in concert with substantial theoretical efforts, particularly by the PARSEC-COLIBRI group, have resulted in a new generation of AGB star models that are anchored to high quality datasets (Marigo et al. 2017; Pastorelli et al. 2019, 2020) and contemporary stellar physics. These models employ far more sophisticated physics than their predecessors, such as the seminal Padova models (Marigo & Girardi 2007; Marigo et al. 2008), which were the first to include a range of physical processes during the thermal pulsating (TP) AGB phase. These effects include the third dredge-up, hot-bottom burning, low-temperature opacity changes, C-to-M star transitions, mass loss, and pulsation. More recently, the Padova group introduced the COLIBRI code in Marigo et al. (2013), which built upon and eventually succeeded the Padova isochrones for AGB stars. The COLIBRI models were further improved using NIR resolved star observations of AGB stars in nearby dwarf galaxies (Rosenfield et al. 2014, 2016; Marigo et al. 2017). TP-AGB lifetimes were even more tightly constrained using deep NIR imaging of the Magellanic Clouds from the VMC/VISTA survey, resulting in the current COLIBRI TP-AGB star models that impressively reproduce a number of observational constraints (Pastorelli et al. 2019, 2020).

Here, we take the next step in SFH modeling by combining the COLIBRI AGB star models with the well-tested CMD modeling framework MATCH (Dolphin 2002) in order to measure quantitative SFHs exclusively from NIR observations of AGB stars. MATCH is a widely used, mature CMD fitting code that has been used to measure SFHs for > 100 galaxies from resolved star CMDs (e.g., Skillman et al. 2003; Williams et al. 2009; McQuinn et al. 2010; Monelli et al. 2010; Weisz et al. 2011; Cole et al. 2014; Weisz et al. 2014; Lewis et al. 2015; McQuinn et al. 2015; Skillman et al. 2017; Williams et al. 2017; Savino et al. 2023; Weisz et al. 2023a; McQuinn et al. 2024a,b,c). Though the incorporation of the COLIBRI models into MATCH is challenging (e.g., because of the need to correctly accounting for self-extinction in AGB stars), it provides several important benefits including a well-vetted framework for CMD analysis, robust uncertainty determination, and uniformity with MATCH-based SFHs of nearby galaxies based on optical CMDs, which

we use to validate the reliability of our AGB star-based SFHs.

Using this newly established framework, we take several steps to illustrate the technique in practice. We first fit mock data to illustrate self-consistency in our modeling. We then measure the SFH of M31’s outer disk using ground-based NIR observations. This region was selected to overlap with the PHAT survey (Dalcanton et al. 2012b; Williams et al. 2014, 2023), which measured the spatially resolved SFH of the same region using deep HST optical CMDs (Williams et al. 2017, hereafter W17), providing a useful comparison point for our AGB star-only based SFHs. Finally, we demonstrate the scientific potential of this new method by measuring the spatially resolved SFH of M31’s inner stellar halo using only ground-based NIR CMDs of AGB stars.

With this decade’s revolution of NIR telescopes like the *James Webb Space Telescope (JWST)*, *Euclid*, and the *Nancy Grace Roman Space Telescope (Roman)*, NIR imaging of AGB stars is already becoming abundantly available (Weisz et al. 2023b; Anand et al. 2024a,b; Boyer et al. 2024; Hoyt et al. 2024; Hunt et al. 2024; Lee et al. 2024; Li et al. 2024; Nally et al. 2024; Newman et al. 2024), and is expected to substantially grow in the next decade. Our study lays the foundational groundwork for combining these exquisite NIR observations of AGB stars and their improved stellar models to measure SFHs of galaxies significantly farther than what is currently possible using optical CMDs.

This paper is organized as follows. We summarize the COLIBRI AGB star models in §2. We describe the MATCH-COLIBRI SFH fitting methodology in §3. We introduce our M31 observations, photometry, and ASTs in §4. We undertake self-consistency tests with mock data in §5.1 and then validate our SFHs against PHAT-based SFHs of M31’s disk in §5.2. Finally, we measure the SFH of M31’s inner stellar halo in §5.3, briefly discuss our findings and current limitations of this method in §6. We conclude by outlining future prospects of SFHs based on resolved AGB star CMDs in the NIR in §7.

Throughout this paper, we adopt the following M31 geometric parameters used by the PHAT team: center R.A. and Declination = (00^h42^m44^s.3, +41°16′09″) and P.A. = 38° (McConnachie et al. 2005; Barmby et al. 2006). We assume the inclination angle of M31 to be 78° (Nieten et al. 2006). Unless otherwise noted, we use projected distances in M31.

2. AGB THEORETICAL ISOCHRONES

We begin with a brief review of theoretical predictions for AGB star properties on the HR diagram and on a NIR CMD from the COLIBRI models. Throughout

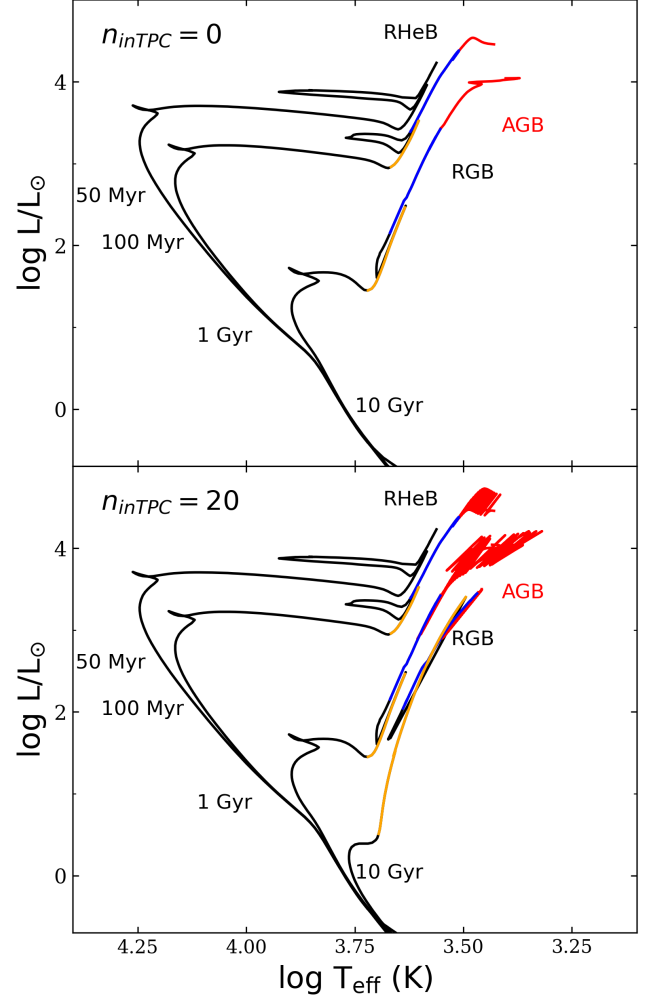


Figure 1. Hertzsprung-Russell diagram for four different PARSEC-COLIBRI isochrones with metallicity $[M/H] = 0.0$ dex. The TP-AGB evolutionary stage is shown in red, the E-AGB phase is shown in blue, and the RGB phase is shown in orange. The top panel shows AGB models with the number of AGB star thermal pulse cycles $n_{\text{inTPC}} = 0$ and the bottom panel shows AGB models with $n_{\text{inTPC}} = 20$.

this paper, we use the COLIBRI version S_37 isochrones (CMD version 3.7; Bressan et al. 2012; Chen et al. 2015, 2014; Tang et al. 2014; Marigo et al. 2017; Pastorelli et al. 2019, 2020).¹

Figure 1 shows select PARSEC-COLIBRI isochrones for select ages between 50 Myr and 10 Gyr. The top panel shows an HR diagram with the number of AGB star thermal pulse cycles (TPC) set to $n_{\text{inTPC}} = 0$, while the bottom one has $n_{\text{inTPC}} = 20$. The latter value is recommended by Marigo et al. (2017) for realistic resolved

¹ <http://stev.oapd.inaf.it/cgi-bin/cmd>

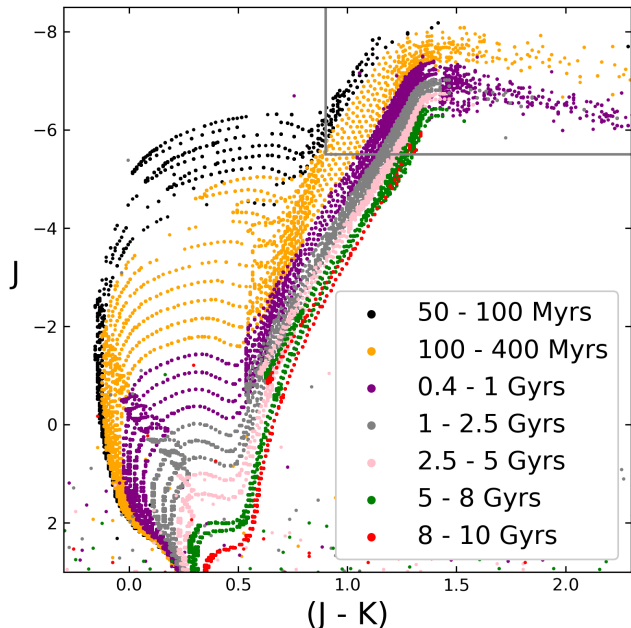


Figure 2. Simulated CMDs using PARSEC-COLIBRI models that demonstrate the power of AGB stars (highlighted within the grey box) as age indicators from ~ 100 Myr to ~ 8 Gyrs. All CMDs were constructed using a constant SFR ($0.1 M_{\odot} \text{ yr}^{-1}$) with a constant metallicity of $[M/H] = 0.0$ dex. The stars are color coded by age. In contrast, other bright stars like RGB stars with ages 5-10 Gyrs can overlap in magnitude and color, making them poor age indicators.

stellar populations analysis. We discuss this point further below.

Young AGB stars are typically the more luminous cool stars on the HR diagram. Though they become less luminous with age, even the 10 Gyr AGB stars are generally more luminous than the TRGB, an important observational property. Moreover, unlike the RGB, the change in AGB age as a function of luminosity (i.e., the age gradient on the HR diagram) is much more pronounced for AGB stars than RGB stars.

The AGB is separated into two stages: the early AGB (E-AGB) and thermally-pulsating AGB (TP-AGB). In the E-AGB, the source of energy is the He-burning shell, whereas for in the TP-AGB, the H-burning shell and He-burning shell ignite in alternating pulses (Habing & Olofsson 2003). All AGB stars begin in the E-AGB phase, where their luminosities increase and temperatures decrease monotonically as a function of time (Iben & Renzini 1983). In the HR diagram, RGB and E-AGB stars of different ages are difficult to separate in the same area of the CMD (Gallart et al. 2005), as shown in Figure 1. Hence, much of our SFH information is derived from TP-AGB stars, except for the very oldest ages for which both E-AGB and TP-AGB stars provide leverage.

The age range we plot is for illustrative purposes only. AGB stars can exist down to ~ 100 Myr in age; below this age, stars do not progress through the AGB star phase. For the very oldest ages ($\gtrsim 10$ Gyr ago), age information comes primarily from E-AGB stars, as lower mass stars generally do not go through the TP-AGB phase. As shown in Figure 1, there is decreased separation between the RGB, E-AGB, and TP-AGB (when present) phases at older ages. In principle, it is possible to measure SFHs using only AGB stars back to ~ 14 Gyr ago, but such ancient time modeling needs to be empirically tested and is beyond the scope of this paper.

Figure 2 shows a NIR CMD, containing stars with a variety of ages at a fixed metallicity of $[M/H] = 0.0$ dex. A modest amount of simulated noise has been added to the CMD to illustrate the AGB stars of different ages are readily distinguishable in a NIR CMD. Specifically, we generated and applied ASTs with a 50% completeness level at $M_J = 7$ mag. The location of AGB stars in the $J - K$ color combination is highlighted by the grey box, which approximately denotes the location of the AGB stars as defined in the COLIBRI stellar isochrones. These same AGB stars are not easily distinguished from RGB stars at optical wavelengths, as we illustrate in later in the context of M31. Even in the red-optical (e.g., 8000 Å), the SEDs of AGB stars are largely indistinguishable from RGB stars; shifting to even bluer wavelengths makes separation of RGB and AGB stars less tenable. The $1 - 3 \mu\text{m}$ wavelength range appears optimal for isolating AGB stars on a CMD.

There are clearly fewer AGB stars than RGB stars. Marigo et al. (2017) predict that $\sim 10^{-3}$ AGB stars form per unit stellar mass. Thus, while AGB stars are more age-sensitive than RGB stars and much brighter than comparably age-sensitive MSTO and SGB stars of the same age, there are fewer of them. We estimate the minimum number of AGB stars for accurate CMD modeling in Appendix A. Finally, we note that ‘extreme’ AGB stars (i.e., the reddest AGB stars), which suffer from particularly complex physics (e.g., rapid and irregular mass-loss, circumstellar extinction), are so rare that they do not meaningfully contribute to the SFH determinations we describe in this paper.

In Figure 3 we show the behavior of AGB stars with a range of metallicities at a fixed age of 1 Gyr. Though there is clearly some dependence on metallicity, the influence of age is much more pronounced. Figure 10, and an associated discussion, in Marigo et al. (2017) provides a deeper demonstration of this point.

3. METHODOLOGY

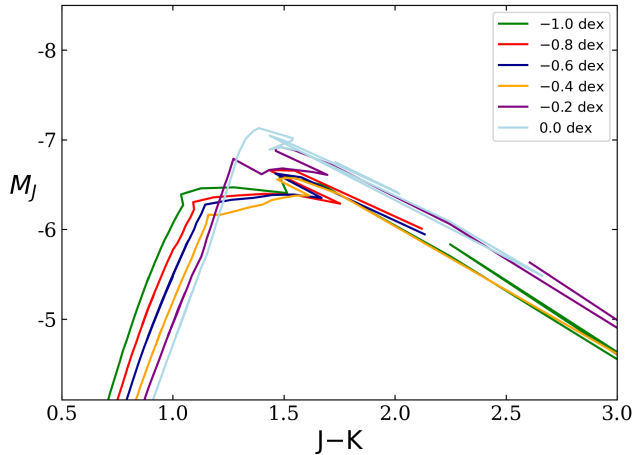


Figure 3. COLIBRI isochrones of the asymptotic giant branch with a constant age of 1 Gyr and a range of metallicities. Metallicity has a modest affect on AGB star positions in a NIR CMD compared to age.

Having provided a qualitative foundation for the age sensitivity of AGB stars in the NIR, we now describe the process by which we formally model AGB stars on a NIR CMD to measure a SFH.

To fit the observed CMDs, we employ the widely-used CMD fitting package *MATCH* (version 2.7, [Dolphin 2002, 2012, 2013](#)). Given a set of stellar models, a specified initial mass function (IMF), and a unresolved binary fraction, *MATCH* creates and linearly combines simple stellar population (SSP) models to create a composite CMD. It then convolves the composite CMD with a noise models (i.e., bias, scatter, completeness) from ASTs to create a model CMD with the same observational effects as the data. The model and observed CMD are converted into Hess diagrams (i.e., a binned CMD) and compared using a Poisson likelihood function. *MATCH* then iterates through various weights of the SSP basis functions until the overall likelihood function is maximized. The synthetic model CMD that best matches the observed CMD is used as the best fit SFH. Random uncertainties on the SFH are computed using a Markov chain Monte Carlo approach, as we describe below.

Because of the complexity of AGB star models (i.e., the need for self-extinction corrections and challenge in defining equivalent evolutionary points), we cannot use *MATCH*’s native SSP model construction framework with the COLIBRI stellar models. Instead, we construct custom SSP models in the desired filters directly from COLIBRI isochrones and then use these pre-constructed models within *MATCH*’s CMD modeling framework. Aside from SSP model construction, the remainder of the CMD fit is virtually identical to the commonly used modes of *MATCH* described here and else-

where in the literature (e.g., [Dolphin 2002; Skillman et al. 2003; Weisz et al. 2014](#)).

Starting from the COLIBRI models, we generate a grid of SSP models, each with a total stellar mass of $10^8 M_{\odot}$ (which yields $\gtrsim 10^4$ AGB stars), spanning a range of ages and metallicities. Our SSP models have ages from $\log(t) = 8.0 - 9.9$ dex (100 Myr to 7.9 Gyr in linear time), logarithmically spaced by 0.1 dex. In principle, we could generate AGB stars models back to 14 Gyr ago for SFH determination. However, we stop at a younger lookback time to match the PHAT SFH we use to empirically validate our method, as described in § 5.2. We adjust the metallicity range of our grid depending on the considered dataset (see § 5.2 and 5.3).

Following recommendations from [Marigo et al. \(2017\)](#) for ‘detailed population studies aimed at accurately reproducing star counts,’ we set $n_{\text{inTPC}} = 20$ (i.e., the number of thermal pulse cycles). For comparison, and as highlighted in Figure 1, isochrones with $n_{\text{inTPC}} = 0$ contain only the quiescent points of the TP-AGB phase (i.e., any luminosity variations from the helium shell flashes are hidden). As discussed in [Marigo et al. \(2017\)](#), isochrones with $n_{\text{inTPC}} = 5$ already contain the most important feature of the thermal pulses: the long-lived low luminosity dips. Thus, the use of $n_{\text{inTPC}} = 5$ is likely sufficient for accurate SFH construction. Nevertheless, we compute isochrones with $n_{\text{inTPC}} = 20$, as it only requires a modestly longer amount of time to compute and it yields slightly more accurate models. Further discussion of how the AGB models change with n_{inTPC} can be found in [Marigo et al. \(2017\)](#).

We generate the SSPs using a Kroupa IMF ([Kroupa 2001](#)) and assume only single stars. The latter is generally a poor assumption of most parts of the CMD. However, a two-AGB binary system is unlikely, owing to their rarity, and their high luminosities, particularly in the NIR, mean that other binary combinations (e.g., AGB-MS star binary) do not significantly affect their colors and luminosities.

Finally, we generate models with a Reimers mass loss value of $\eta = 0.2$ for RGB stars. For our fiducial models we adopt the default value recommended by PARSEC-COLIBRI, and discuss variations in this choice in §6.

We import these models into *MATCH* in the desired filter set and use them to fit the observed CMD. After determination of the best fit SFH, we calculate random uncertainties on the SFH using a hybrid Monte Carlo (HMC) approach implemented by [Dolphin \(2013\)](#), following guidance from other papers in the literature that use this approach in *MATCH* (e.g., [Rosenfield et al. 2016;](#)

Williams et al. 2017; Lazzarini et al. 2022; McQuinn et al. 2024a).

Many of the SFHs measured from CMDs in the literature also feature systematic uncertainties (e.g., Weisz et al. 2011; Lazzarini et al. 2022). These are designed to capture variations on the SFH due to choice of stellar model (Dolphin 2012) and other inputs (e.g., Savino et al. 2023). The method for computing systematic uncertainties has been well-calibrated for optical CMDs of different depths using multiple stellar evolution models. However, because the COLIBRI models are the only models with the appropriate level of detail necessary for TP-AGB modeling, an inter-method comparison is currently not possible. For example, Marigo et al. (2017) includes a comprehensive discussion (see their Section 3.8, Figure 11) comparing the COLIBRI isochrones of the TP-AGB phase with the BaSTI, Padova, and MIST isochrones. In brief, the BaSTI isochrones lack the M to C-type AGB star transition, the Padova isochrones miss details related to mass loss, thermal pulse cycles, and hot-bottom burning, and the MIST isochrones apply M-type molecular opacities to C-type stars, leading the C-type stars to be significantly hotter/bluer than the C-type stars in the COLIBRI isochrones. Consequently, throughout this paper, we are only able to consider random uncertainties. We discuss the issue of systematic uncertainties further in §6.

4. DATA

For all AGB-based SFHs in this paper, we use J and K images from the Wide Field Camera (WFCam), on the 3.8 m United Kingdom InfraRed Telescope (UKIRT), taken from 2005 to 2008. The data were reduced through the Cambridge Astronomy Survey Unit (CASU) WFCam pipeline (Irwin et al. 2004; Hodgkin et al. 2009), which provides chip-by-chip point-spread-function photometry calibrated to the Two Micron All Sky Survey (Skrutskie et al. 2006), along with source classification (i.e., stellar vs. non-stellar)². This catalog was then further processed by Ren et al. (2021) for a study on red supergiants in M31. They combined all the measurements on a filter-by-filter basis by averaging the photometry for multiple measurements of the same stars. This photometry covers over 30 kpc in projected radii across the face of M31, providing excellent coverage of AGB stars across M31’s inner stellar halo.

² <http://casu.ast.cam.ac.uk/surveys-projects/wfcam>

From the raw source catalogs, we keep only sources classified as stellar in both J and K by the CASU pipeline. We then clean the final catalogs using photometric quality cuts that are demonstrated in the panels of Figure B1. We use a constant+exponential function to cull the data via the photometric uncertainty as a function of the J-band and K-band magnitudes. The specific functional form of these cuts can be found in Appendix B.

We generate ASTs to characterize the biases, uncertainties, and completeness of our data using the procedure described in Ren et al. (2024). We run ASTs across the PHAT footprint. However, because of the wide areal coverage of the halo data (~ 7.5 degrees²), running ASTs for each position of the UKIRT footprint is prohibitively computationally expensive in the framework of this photometric routine. Instead, we run ASTs in five representative stellar density ranges, using stellar density as an indicator of the expected crowding (and resulting photometric noise) in each range. We then measure the average stellar density of the 18 halo regions discussed in §5.3. We use the set of ASTs that were generated for regions of similar stellar density. Table 1 lists the properties of the ASTs used. The process of generating ASTs in select regions of specific stellar density and applying them more broadly is also used by the PHAT/PHATTER teams, who faced a similar computational challenge of running ASTs across the entire extent of their M31 and M33 footprints, respectively (Williams et al. 2017; Lazzarini et al. 2022). We summarize our ASTs in Table 1.

5. STAR FORMATION HISTORIES

5.1. Application to Mock Data

As a first test of our method for self-consistency, we generate synthetic CMDs for a variety of SFHs using our basis functions and simulated ASTs. For our noise model we generate artificial stars with 50% completeness limits in J and K at 27 mag using the `makefake` function in `MATCH`. These fake ASTs only include the effects of photon noise and not crowding.

To measure the AGB star SFH, we run `MATCH` on the ‘observed’ CMDs shown in Figure 4. We adopt an age range of $\log(t) = 8.0$ to 9.9 with a spacing of 0.1 dex and a metallicity range of $[M/H] = -0.4$ to 0.0 dex with a spacing of 0.1 dex. We use well-populated basis functions ($\sim 10^8 M_\odot$) to minimize any effects of Poisson variations, which are the not purpose of this test.

Next, we run the simulated CMDs through `MATCH` as if they were real photometric datasets. We then compute random uncertainties using HMC. We ran an exhaustive set of simulations with various SFHs. For brevity, we

Table 1. UKIRT 50% Completeness Limits over a Range of Stellar Densities

Stellar Density [stars arcmin ²]	J [mag]	K [mag]	Number of AGB ASTs used ^a	Regions
0 – 6	19.4	18.4	183605	1, 2, 9, 10, 12, 13, 14, 15, 16
6 – 10	19.3	18.4	477373	3, 11, 17, 18
10 – 13	19.3	18.4	881304	7
13 – 16	19.3	18.4	550815	4, 8
16 – 19	19.2	18.4	587536	5, 6

^aStars with injected magnitudes of $J < 20$ mag, i.e., 1 mag fainter than our AGB selection.

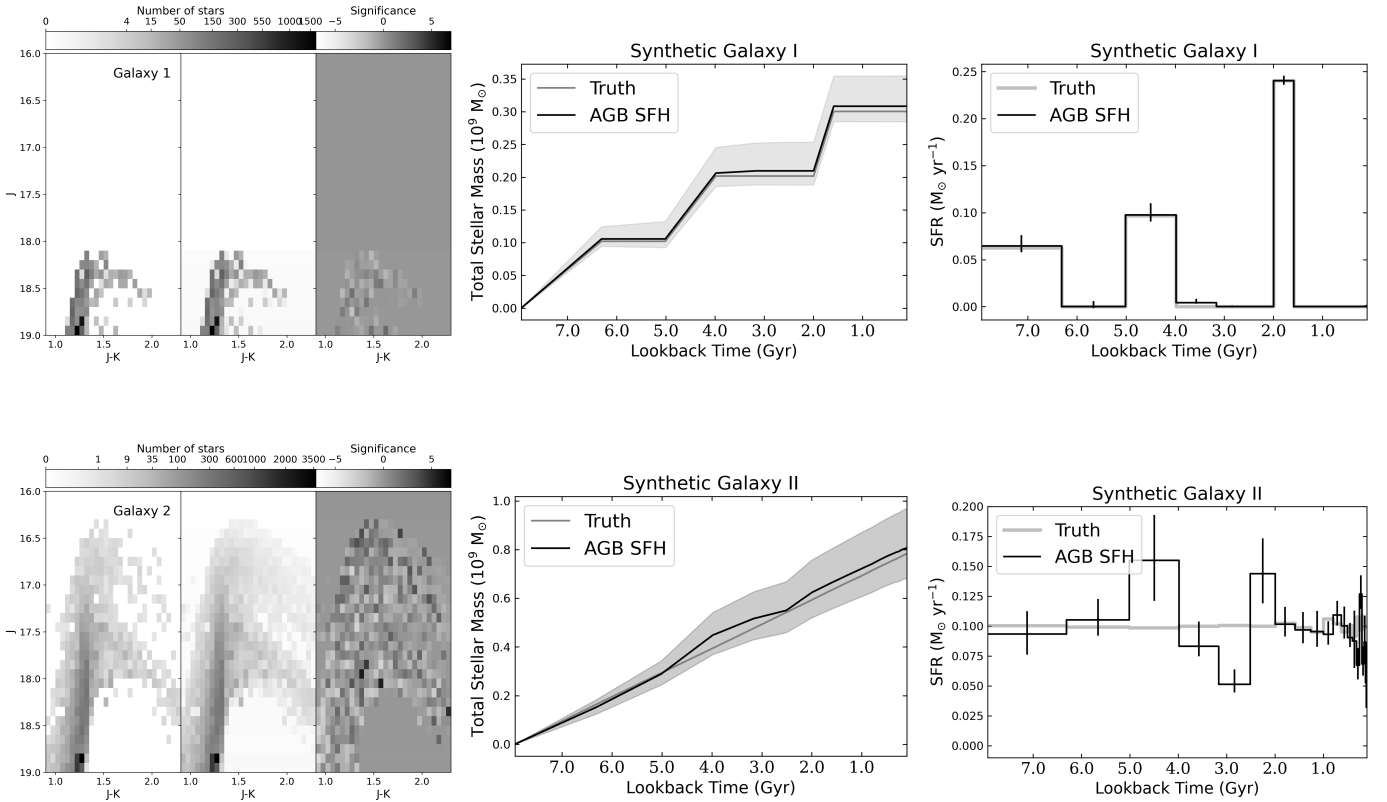


Figure 4. Comparisons between our ‘injected’ star formation histories and ‘recovered’ star formation histories in the two mock galaxies described in §5.1. (Left) Density maps for the observed, best-fit, and residual CMDs, expressed in units of Poisson standard deviations. (Middle) Cumulative stellar mass formed as a function of time. (Right) Total star formation rate as a function of time. These tests illustrate our ability to self-consistently recover SFHs from AGB stars.

only explore a couple of illustrative examples below for a constant and bursty SFH. However, the conclusions are the same no matter in the input SFH: **MATCH** self-consistently recovers the input SFH using mock data.

Synthetic Galaxy I: Multi-burst SFH. Synthetic galaxy I was created from three star formation bursts

with ages of 2.0, 5.0, 7.9 Gyr and metallicities $[M/H] = -0.4, -0.2, 0.0$ dex, respectively. Each burst forms a stellar mass of $10^8 M_\odot$. In the top panel of Figure 4, we show the “observed” CMD, recovered best fit model CMD, and residual CMD, along with the recovered and input star formation histories.

Synthetic Galaxy II: Constant SFH. Synthetic galaxy II was created using a roughly constant star formation rate of $0.1 M_{\odot}/\text{yr}$ from $\log(\text{age})=8.0$ to 9.9 dex at a fixed metallicity of $[M/H]=0.0$ dex. In the bottom panel of Figure 4, we show the “observed” CMD, recovered best fit model CMD, and residual CMD, along with the recovered and input star formation histories.

The excellent agreement between all input and recovered tests indicates that MATCH is self-consistently able to handle our custom basis functions. We now turn to application of this method to real data.

5.2. Comparison to PHAT

A further check on consistency is to compare our AGB star-based SFHs to those derived from deep optical CMDs. Ideally, we would use an optical CMD that reaches the oldest MSTO to provide an anchor for this testing.

However, only datasets that are suitably deep, outside the Magellanic Clouds that have been used to calibrate the AGB models, are from small-area HST or JWST fields (e.g., Skillman et al. 2003; Dolphin et al. 2003; Brown et al. 2006; Geha et al. 2015; Albers et al. 2019; McQuinn et al. 2024a) or from ground-based imaging of MW satellites (e.g., de Boer et al. 2011, 2012a,a, 2014; Muñoz et al. 2018). At issue is that these fields do not contain a suitable number of AGB stars (at least ~ 700 , as we discuss below) to enable a reliable SFH.

We instead opt to compare our AGB star-based SFH to those measured as part of the PHAT survey. Specifically, we use the SFH fits from W17, who measured the spatially resolved ancient SFH of the PHAT region from optical CMDs that extend to ~ 2 mag below the RC, as shown in Figure 5. Although these CMDs do not reach the 10 Gyr MSTO, and instead rely on advanced phases of evolution (e.g., the position and shape of the RC), W17 took great care to validate their results against CMDs taken throughout M31’s disk that did reach the oldest MSTO (Bernard et al. 2015a,b). We did consider comparing results directly to other M31 SFHs that do reach the oldest MSTO (Brown et al. 2006; Bernard et al. 2015a), but there are not enough AGB stars in the spatially matched HST footprints. Similarly, we considered a comparison to the larger number of fields from Richardson et al. (2008), but (a) they do not provide quantitative SFHs and (b) we are again limited by the number of AGB stars in a given field.

Recognizing the limitations of their moderately deep CMDs, W17 adopt a single ancient age bin of 8-14 Gyr ago. They adopt a finer time resolution (0.1 dex) for ages younger than ~ 8 Gyr. Therefore, for comparison purposes, in this paper we only measure the AGB-based

SFHs back to 8 Gyr ago. We stress this age limit is not inherent to the AGB star SFH method itself, but rather due to our desire for empirical validation.

5.2.1. Photometric Selection

Beyond an age restriction, we limit this comparison to the outer region ($D_{\text{deprojected}} > 11$ kpc) of the PHAT survey, as illustrated in Figure 6. This enables us to compare to the deepest optical data available, avoids the need to model the complex spatially varying differential extinction that dominates most of M31’s inner disk (e.g., Dalcanton et al. 2015; Lewis et al. 2015). It also mitigates the impact of crowding on the optical CMDs and hence the SFHs. Crowding significantly impacts the depth of the optical CMDs in M31’s inner disk, reducing the fidelity of the W17 SFHs. We note that while crowding affects the faintest stars in the the PHAT survey, it has minimal impact on brighter stars. For example, Figure 6 in Gregersen et al. (2015) demonstrates the RGB stars with $D_{\text{deprojected}} \gtrsim 11$ kpc have $\geq 90\%$ completeness.

For $D_{\text{deprojected}} \gtrsim 11$ kpc, the PHAT CMD has ~ 47 million stars (Figure 5). Of these stars, ~ 33 million are located above the 50% completeness limit of $F814W \sim 26.5$ and were used by W17 to measure the spatially resolved SFH of this region. We sum the SFH of each region in this area as provided in the W17 paper.

In comparison, our AGB star-based SFH contains $\sim 23,000$ AGB stars that are located within the selection box in Figure 5, which is defined on the faint end by the 50% completeness limit of our data ($J = 19.0$ mag). Unlike the the PHAT optical CMDs, our AGB star data are not generally crowded in any part of M31. The 50% completeness limit in the inner regions ($D_{\text{deprojected}} \lesssim 11$ kpc) is only ~ 0.5 mag brighter than in the outskirts. The significantly reduced sensitivity to crowding is another strength of AGB stars in the NIR for SFH determinations.

Having defined the spatial area of our sample, we next correct our NIR data for reddening. Even in the NIR, internal reddening in M31’s outer disk is not negligible. The dust map generated by Dalcanton et al. (2015) represents one of the highest-resolution reconstructions of M31’s internal reddening. Unfortunately, it is not publicly available necessitating a different means of applying a reddening correction.

We opt to use the Draine et al. (2014) dust map, which is based on far-infrared and submillimeter emission observations from the *Spitzer Space Telescope* and *Herschel Space Observatory*. The Dalcanton et al. (2015) reddening map predicts $\sim 2.5\times$ less extinction than the Draine et al. (2014) dust map, although their overall

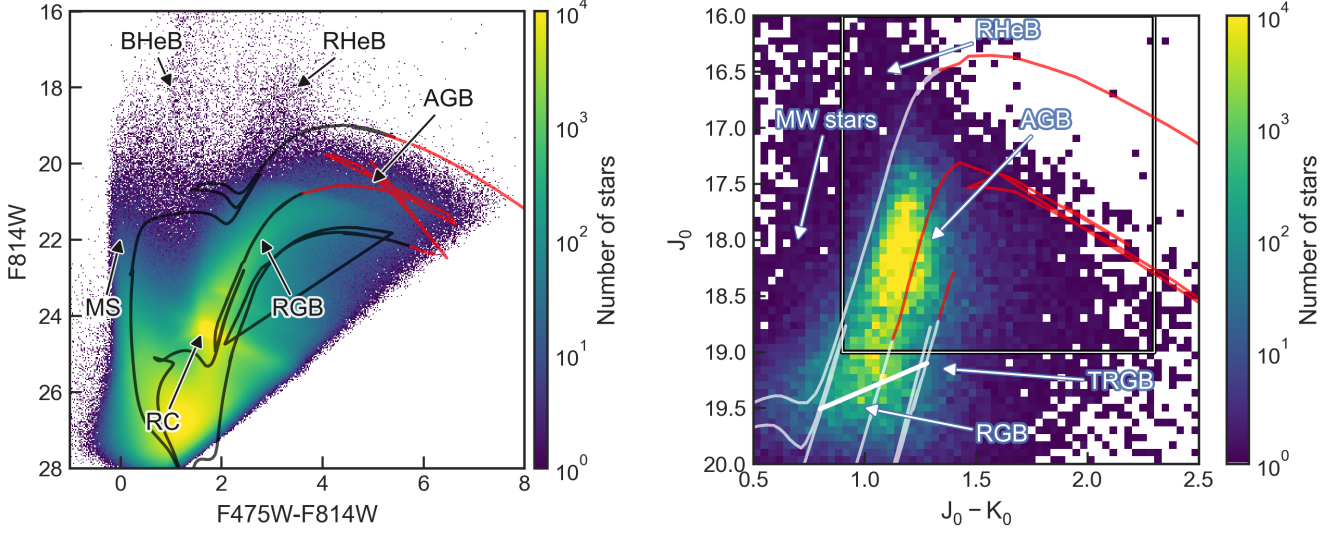


Figure 5. (Left) CMD of the PHAT optical data analyzed in W17 for $d > 11$ kpc. (Right) CMD of our UKIRT data that overlaps with the PHAT footprint analyzed in W17 for $d > 11$ kpc. Color indicates the number of data points in each CMD bin. The grey box shows our selection criteria for the AGB stars, which also corresponds to the grey box in Figure 2, shifted to M31’s distance. In both CMDs, isochrones of 100 Myr, 1 Gyr, and 8 Gyr with a metallicity of $[M/H]=0.0$ dex are overlaid with the AGB evolutionary phase highlighted in red. The PHAT optical CMD contains ~ 47 million stars of which ~ 33 million stars are above the 50% completeness ($F814W \approx 26.5$ mag). Our NIR CMD contains $\sim 43,000$ stars and a 50% completeness limit of $J = 19.0$ mag. Our selection region contains $\sim 23,000$ AGB stars from which we measure our SFH.

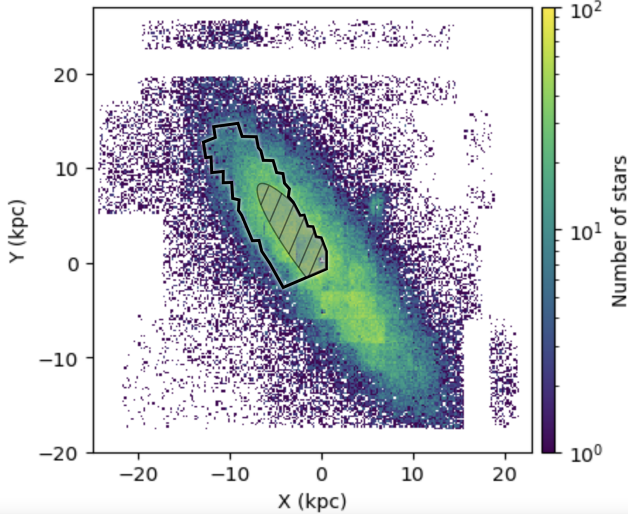


Figure 6. Spatial map of $\sim 175,000$ AGB stars from our UKIRT data over the entire region of M31 covered by our data. The PHAT footprint is overlaid in black. We excluded data inside a deprojected radius of $d = 11$ kpc, denoted by the shaded grey hatched ellipse, to avoid the crowded and reddened inner regions of M31’s disk that significantly affect the optical CMD. The PHAT SFH was based on ~ 33 million stars while our AGB-star SFH of the same region used only $\sim 23,400$ stars.

morphological agreement is excellent. Thus, we use the Draine et al. (2014) map with the Dalcanton et al. (2015) corrections. Specifically, the Dalcanton et al. (2015) corrects the Draine et al. (2014) maps by dividing by a factor of $R = 2.53$ and then an additional additive correction of $b = -0.04$ to account for possible systematic biases. This transformation is then as follows: $A_{V,Draine}/A_{V,Dalcanton} = 2.53(1 + 0.04/A_{V,Dalcanton})$.

We then convert to A_J and A_K using $A_J = 0.282A_V$ and $A_K = 0.114A_V$ (Cardelli et al. 1989). We find the average reddening correction from the Draine et al. (2014) maps in the PHAT footprint outside a radial distance $D > 11$ kpc to be $A_J = 0.20$ mag, and $A_K = 0.08$ mag. We apply this average correction to our photometry. For reference, the foreground Milky Way extinction toward M31 is $A_J = 0.05$ mag, and $A_K = 0.02$ mag, calculated from the Schlegel et al. (1998) dust maps recalibrated by Schlafly & Finkbeiner (2011), assuming the Cardelli et al. (1989) reddening law with $R_V = 3.1$.

Figure 5 shows a comparison between the HST-based optical CMD of M31 at $D > 11$ kpc (left) and our ground-based NIR CMD of the same region (right). As discussed in §2, it is virtually impossible to separate out AGB and RGB stars in the optical. This point is reinforced by the optical PHAT CMD.

In the NIR, we select AGB stars as having colors between $0.9 < (J - K) < 2.3$ mag and magnitudes between $16 < J < 19$ mag based on the locations AGB stars isochrones. This selection also eliminates contamination from red supergiants and foreground stars, both of which are bluer than our selection region. We also limit the AGB stars as having magnitudes brighter than the TRGB ($J = 19$ mag), which is also the 50% completeness limit of our data.

In total, there are ~ 33 million stars in the PHAT region above a magnitude of $F814W = 26.5$ mag (the 50% completeness limit) used to measure the SFH, compared to just 23,400 AGB stars used to measure our SFH. We emphasize that most of the age information in the PHAT SFHs is from the position of the red clump at $F814W \approx 24.2$ mag, whereas we only used AGB stars brighter than $J \lesssim 19$ mag in NIR wavelengths.

5.2.2. Measuring the AGB Star-based SFH in the PHAT Region

To measure the AGB star SFH, we run MATCH on stars within the grey box in the UKIRT CMD shown in Figure 5. We adopted an age range of $\log(t) = 8.0$ to 9.9 with a spacing of 0.1 dex and a metallicity range of $[M/H] = -0.4$ to 0.0 dex also with a spacing of 0.1 dex. The metallicity range was motivated by measurements of the RGB star metallicities across M31's disk by the PHAT team (Gegersen et al. 2015), while the age range largely matches that of W17 and the age range permitted by AGB stars.

For our fitting, we adopt an M31 distance modulus of $\mu_0 = 24.47 \pm 0.05$ mag (766 ± 18 kpc; Lee 2023). This distance was derived from the J-region asymptotic giant branch (JAGB) method, a standard candle based on AGB stars, using the same UKIRT photometry studied in this paper. This is virtually identical to the distance modulus assumed by W17 and to other commonly adopted distances to M31 (e.g., Jeffery et al. 2011; de Grijs & Bono 2014; Bhardwaj et al. 2016; Savino et al. 2022). We use a CMD bin size of 0.05×0.10 mag in color and magnitude, respectively. We then follow the CMD modeling procedure described in §3.

Figure 7 shows the SFH of the PHAT region based on AGB stars. From the residual CMDs (left panel), we see that our best fit model provides a good match to the data. This is visually apparent by the general ‘checkerboard’ pattern in the residual significance plot, i.e., the residual weighed in each Hess diagram in units of standard deviations. This plot shows modest discrepancies between the data and model at the bluest colors, but they are of moderate significance and are on-par with the quality of residuals in most optical CMD modeling (e.g., Monelli et al. 2010; Hidalgo et al. 2011; Weisz et

al. 2011, 2014; Skillman et al. 2017; Albers et al. 2019; Savino et al. 2023) and with JWST in the NIR (e.g., McQuinn et al. 2024a,c).

The middle panel shows the cumulative SFH the AGB star-based SFH in black, and the W17 best fit PARSEC-based SFH in red. The uncertainty envelope for both SFHs reflects the 68% random uncertainties. We note that although W17 include AGB stars in their CMD modeling they (a) are of limited utility due to overlap with the RGB and (b) are not fit with the more recent versions of the COLIBRI AGB models, as they were not yet available. As discussed extensively in W17, the age information at most epochs comes from the RC and ratios of RC to RGB stars, with some contribution from AGB stars. The two SFHs, (AGB star and W17) use the same IMF, but adopt slightly different minimum mass limits for the low-mass IMF. This introduces an order of unity difference in the SFHs and stellar masses formed. We apply this small IMF correction to the W17 for the purposes of equal comparison.

The two cumulative SFHs are in excellent agreement. Both show a modest amount of stellar mass formed from $\sim 5 - 8$ Gyr ago, followed by two episodes of enhanced star formation. The AGB SFH has a burst $\sim 4 - 5$ Gyr ago, while the optical SFH shows a less intense burst from $\sim 3 - 5$ Gyr ago. Both formed the same stellar mass over the 3-5 Gyr ago interval. Though the difference in timing is not statistically significant, in future studies it will be interesting to understand if such differences could be due to information content of the data (e.g., ‘bleeding’ of star formation into adjacent time bins due to the increased age-metallicity degeneracy in the RC). The second star formation event is from $\sim 1.5 - 2$ Gyr ago (AGB stars) or $\sim 2 - 2.5$ Gyr ago in the optical. The total stellar mass formed over 8 Gyr by each method is the same.

Random uncertainties on the W17 SFH are larger than for the AGB stars, despite a factor of $1400\times$ more stars used to measure the optical CMD-based SFH. This is most likely due to the reduced age-metallicity-dust degeneracy of the AGB stars in the NIR compared to the combination of the MS, RC, RGB, and AGB stars in the optical.

We further investigated this by comparing the age-metallicity relationships (AMRs) from our fits and W17. We find the AMRs to be nearly identical between the two methods. Both are generally consistent with Solar metallicity, except for a noticeable drop to $[M/H] = -0.4$ at ~ 2 Gyr. Similar decreases in metallicity are measured in other regions of M31's disk (Bernard et al. 2015a) from CMDs that reach the oldest MSTO. This

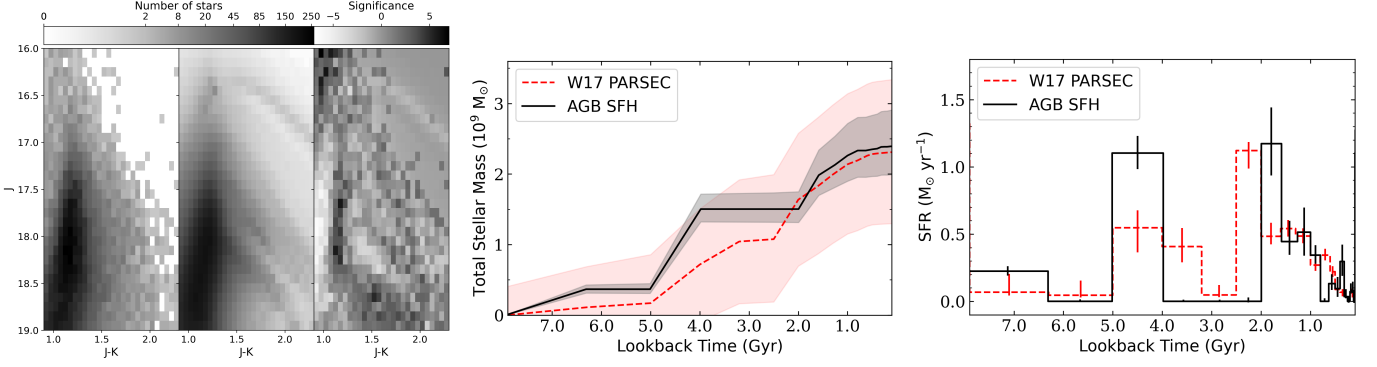


Figure 7. (Left) Hess diagrams for our AGB SFH fit for the observed data (left panel), best-fit linear combination of SSPs (middle panel), and residual CMDs (right panel). The residuals are expressed in Poisson standard deviations. (Middle) Comparison between our measured cumulative stellar mass formed and the W17 measurement using the PARSEC models. (Right) Comparison between our SFR measured from AGB stars and the SFR measured in W17.

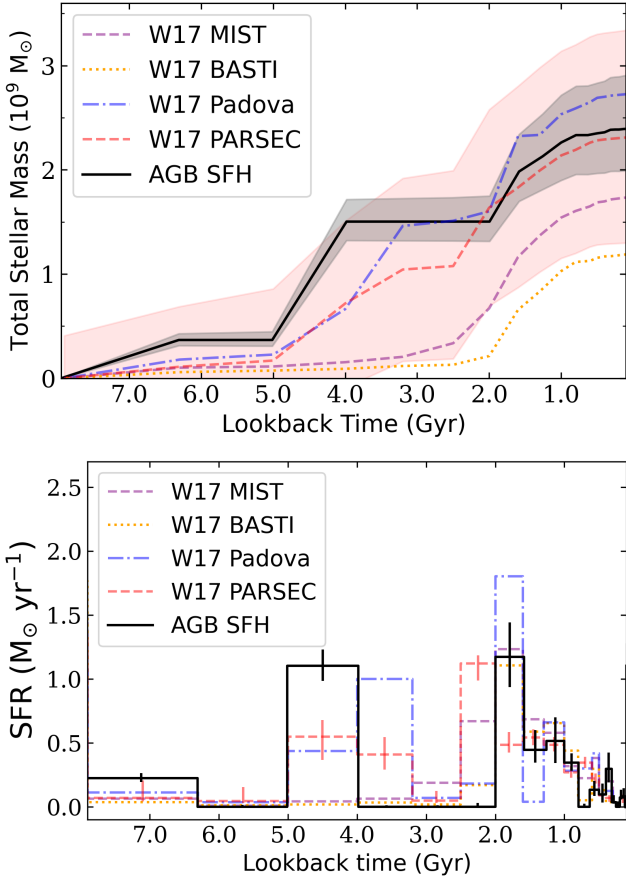


Figure 8. Same plots as Figure 7 now with all model sets from W17.

provides additional confidence in the fidelity of our AGB star-only SFH.

The right panel of Figure 7 shows the differential SFH, i.e., SFR vs time, of the AGB star and PHAT SFHs. As with the cumulative SFHs, we find good agreement be-

tween the amplitude and timing of star formation in both SFHs, though there are a few differences. For example, the timing and amplitude of star formation around $\sim 3 - 5$ Gyr ago and $\sim 1 - 2.5$ Gyr ago are slightly different. As with the cumulative SFHs, such differences in the exact timing of star formation from CMD modeling are often observed when using different stellar models or CMD fitting codes (e.g., Weisz et al. 2011; Dolphin 2012; Cole et al. 2014; Skillman et al. 2017; Savino et al. 2023).

To examine how significant these variations may be, in Figure 8 we compare best fit SFHs measured using different stellar models from W17 with our AGB star-based SFH. It is clear from the cumulative and differential SFHs that our AGB star-only SFH is well within the model-to-model variance from optical CMD analysis. Each of the optical-based SFHs shows the same qualitative trend of stellar mass growth, but with slightly different timings and amplitudes of star formation episodes, as well as modest differences in the total stellar mass formed. Within this context, our AGB-based SFHs are as robust as any of the SFHs based on deeper optical CMDs.

Our measurement is based on $\sim 23,000$ AGB stars. In §A, we quantify how the quality of the fit and statistical errors scale with the number of AGB stars, by measuring the AGB SFH from decreasingly smaller random samples of AGB stars. In Figure A1, we show that as few as 280 AGB stars can deliver a reasonable SFH compared to the W17.

Finally, we note that our NIR CMD of the PHAT region (Figure 5) clearly contains AGB stars that are older than 8 Gyr. While in principle we could extend our analysis to older ages (as discussed in Appendix C), for the sake of empirical verification, we limit this com-

parison to 8 Gyr and will expand our tests to older look back times in future papers, when suitable datasets are available.

5.3. Measuring the SFH of M31’s Inner Halo

We now provide an illustrative use case for our AGB star-only SFH technique by measuring the SFH for the inner stellar halo of M31. M31 is long-known to have a complex stellar morphology and a halo filled with substructure (see [McConnachie et al. 2018](#) and references therein). Measuring the SFH of M31’s stellar halo from AGB stars may help shed new light on its formation history, while also providing a practical showcase for the power of AGB stars for measuring SFHs of stellar halos in other galaxies throughout the local Universe.

5.3.1. Data and Extinction Corrections

Our photometry includes data out to a projected radius of 32 kpc, encompassing M31’s inner stellar halo. We exclude data within a deprojected distance of 20 kpc, as shown in Figure 9, to avoid the complexity extinction in the disk (e.g., [Dalcanton et al. 2015](#)). Within the stellar halo footprint, we now verify the internal reddening derived from the A_J extinction map discussed in §5.3 is very small and does not vary much spatially, using the [Draine et al. \(2014\)](#) map which covers the full range of our UKIRT data in major axis, but not the full range in minor axis. However, the minor axis (northwest and southeast sections of M31’s halo) are expected to contain even less dust. The average extinction values derived from the corrected map discussed in §5.2.1 outside of a deprojected distance of 20 kpc are $A_J = 0.05$ mag and $A_J = 0.02$ mag, which are exactly equal to the foreground Milky Way reddening corrections also discussed in §5.2.1. For simplicity, we apply these small extinction corrections directly to our photometry before modeling the CMD, and then do not solve for extinction as part of the CMD modeling.

Figure 10 shows the NIR CMD of M31’s inner halo we used to measure its SFH ($D_{\text{deprojected}} > 20$ kpc). The grey box indicates the selection region for AGB stars. Select PARSEC-COLIBRI isochrones (0.1, 1, 8 Gyr) are included for reference. There are $\sim 39,000$ AGB stars in this region. The 50% completeness limit across the inner stellar halo is $m_J \approx 19.3$ mag.

5.3.2. Spatial Selection

The large number of AGB stars in M31’s inner halo allow us to measure a spatially resolved SFH. We divide our photometry into 18 spatial regions according to the following criteria. First, as illustrated in Figure 9, we prioritize placing the four major substructures from [McConnachie et al. \(2018\)](#) into separate regions. Regions

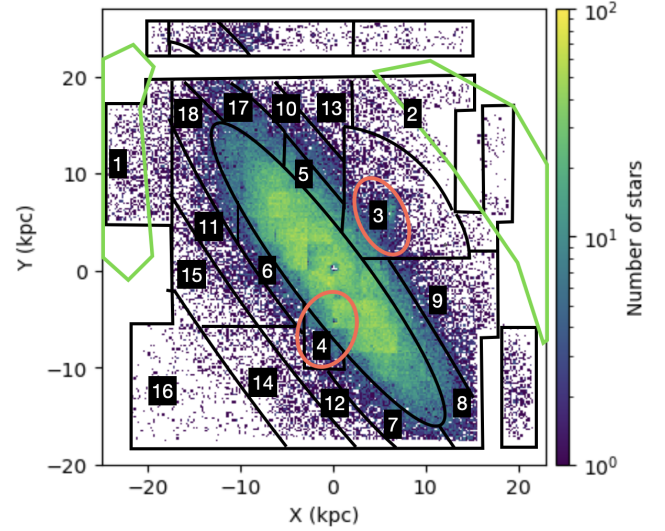


Figure 9. Map of the 18 regions overplotted on an AGB stellar density map of M31. Regions 1-4 were specifically designed to contain the substructures discussed in [McConnachie et al. \(2018\)](#). Region 1 contains the Eastern Shelf, Region 2 contains the Western Shelf, Region 3 contains NGC 205 (M110) and Region 4 contains M32. Green polygons highlight the approximate positions of the the stellar structures which are a part of the Giant Stellar Stream (GSS), and pink ellipses correspond to the two dwarf galaxies in this map. The positions of the AGB stars and their region labels are available as Data behind the Figure.

1 and 2 contain the Eastern and Western Shelves, respectively, which have been identified as being radial “shell” features created from the Giant Stellar Stream (GSS) progenitor’s last pericentric passage ([Ferguson et al. 2002, 2005; Fardal et al. 2006, 2008; Richardson et al. 2008; Fardal et al. 2012; Bernard et al. 2015b](#)). Region 3 contains NGC 205 (M110), a satellite galaxy of M31. Region 4 contains M32, another satellite galaxy of M31. [D’Souza & Bell \(2018\)](#) proposed that M32 is the progenitor of the GSS, whose merger with M31 is thought to be responsible for the burst of global star formation seen in M31’s disk and inner stellar halo ~ 2 Gyr ago. The remaining regions were chosen to have at least 700 AGB stars, which is near the lower limit for the number of AGB stars needed for a robust SFH recovery (see Appendix A). The regions were delineated via a combination of radial and azimuthal lines, resulting in the irregular region shapes seen in Figure 9. The goal for these remaining sections is simply to provide as much resolved spatially information as possible, particularly in the radial direction, in light of other spatial and number of star constraints. The number of AGB stars ranged from ~ 800 AGB stars in region 16 to ~ 4900 AGB stars in region 3.

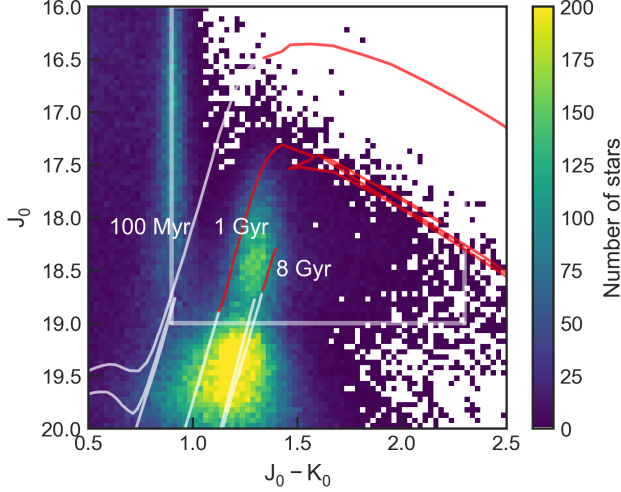


Figure 10. CMD of our UKIRT data outside of a deprojected radius of 20 kpc. Color indicates the number of data points in each place in the CMD. The grey box shows our selection criteria for the AGB stars. Isochrones of 100 Myr, 1 Gyr, and 8 Gyr with a metallicity of $[M/H] = 0.0$ dex are overlaid with the AGB evolutionary phase highlighted in red.

5.3.3. Star Formation History

We run *MATCH* on each of the 18 spatial sub-regions. In each instance, we adopt an age range of $\log(t) = 8.0$ to 9.9 dex with a spacing of 0.1 dex and a metallicity range of $[M/H] = -1.4$ to 0.0 with a spacing of 0.2 dex. We compute random uncertainties for each region following using the HMC approach described in §3.

Figure 11 and Figure 12 show the differential and cumulative SFHs for each region. We note that there is fairly sizable variation in timing, duration, and amplitude of the SFHs as a function of position. Because the inner stellar halo of M31 is dominated by sub-structure, and not a clear smooth component, it is perhaps not surprising to see such variations in the SFHs and stellar mass growth as the inner halo was assembled from many individual pieces, each with their own formation histories.

In general, we find that most regions have prominent star formation from $\sim 4 - 5$ Gyr ago and again $\sim 1 - 2.5$ Gyr ago. Many also exhibit some level of star formation at ages of < 1 Gyr. In terms of cumulative stellar mass growth, there is a factor of ~ 3 difference in the mass formed in the least (region 13) and most (region 3) active regions. Region 3 contains NGC 205, while region 13 contains among the least amount of sub-structure according to the maps in [McConnachie et al. \(2018\)](#). It may be the closest we come to sampling the smooth underlying halo of M31. Other sparse-looking regions (e.g., 14 and 16) are located in the direction of

the GSS. Expanding the NIR imaging and/or applying this method to other wide-field NIR imaging of M31 is an obvious path forward to exploring the SFH of its stellar halo at larger radii and to providing broader context with which to interpret our SFHs.

In Figure 13, we plot the spatially-resolved SFH of M31’s inner stellar halo. Each of the 18 regions is color-coded by the best fit SFR at select lookback times. We note several interesting features. First, the most active regions are 3 and 8. Region 3 (NGC 205) shows prominent star formation $\sim 7, 4.5$ and 2 Gyr ago, while region 8 also shows activity at ~ 4.5 and 2 Gyr ago. Region 16, which is in the direction of the GSS, has its highest activity levels from $\sim 2 - 3$ Gyr ago. An inner “ring” of regions ($D_{\text{projected}} \sim 25$ kpc) all show enhanced activity ~ 4.5 Gyr ago. Interestingly, we see little evidence of star formation in most regions at ages $\gtrsim 5$ Gyr ago, aside from around NGC 205, and very little activity at ages < 1 Gyr ago.

Figure 14 shows the global SFH of M31’s inner halo (i.e., all 18 regions summed together), along with the corresponding 68% uncertainties. The overall shape of the SFH is similar to many of the individual regions, with modest star formation $\sim 6 - 8$ Gyr ago, a prominent burst $\sim 4 - 5$ Gyr ago, and steady and variable star formation from $\sim 0.1 - 2$ Gyr ago. Our global SFH shows that over the past ~ 8 Gyr, the inner stellar halo of M31 formed $\sim 4 \times 10^9 M_{\odot}$, $\sim 50\%$ of which appears to have occurred $\sim 4 - 5$ Gyr ago.

M31’s inner stellar halo is thought to be predominantly composed of substructure from past interactions (e.g., [McConnachie et al. 2018](#), and references therein). We briefly discuss our spatially resolved SFHs in relation to some of the known substructures within M31’s inner stellar halo and then comment on the global formation history of the halo. We publish our spatially resolved SFHs as part of this paper in order to facilitate further investigation by the community.

Figure 13 shows clearest enhancements in SFR $\sim 4 - 5$ Gyr ago. The highest SFRs at this time include the present day location of NGC 205 (region 3) and the area adjacent to it that extends to the south (region 8). The SFH of NGC 205 measured from deep HST optical imaging shows a similar enhancement in star formation activity ~ 5 Gyr ago ([Savino et al. in prep](#)). Older studies of NGC 205’s stellar populations qualitatively support the presence of intermediate age and even young stellar populations in NGC 205’s central region (e.g., [Richer et al. 1984](#); [Lee 1996](#); [Davidge 2003, 2005](#); [Rose et al. 2005](#); [Sharina et al. 2006](#); [Monaco et al. 2009](#)). To the best of our knowledge, there are no other SFHs overlapping region 8 in the literature.

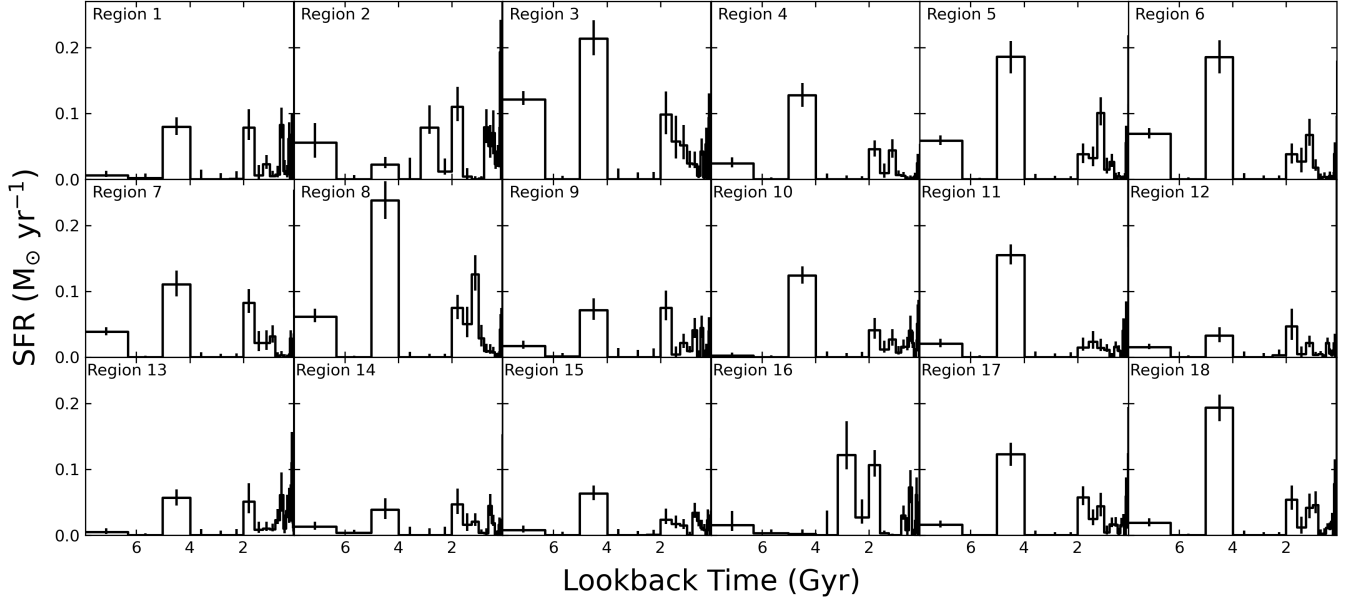


Figure 11. Star formation rate for the past 8 Gyr in the 18 regions, which are labeled in Figure 9. The star formation rates and their uncertainties of each region are available as Data behind the Figure.

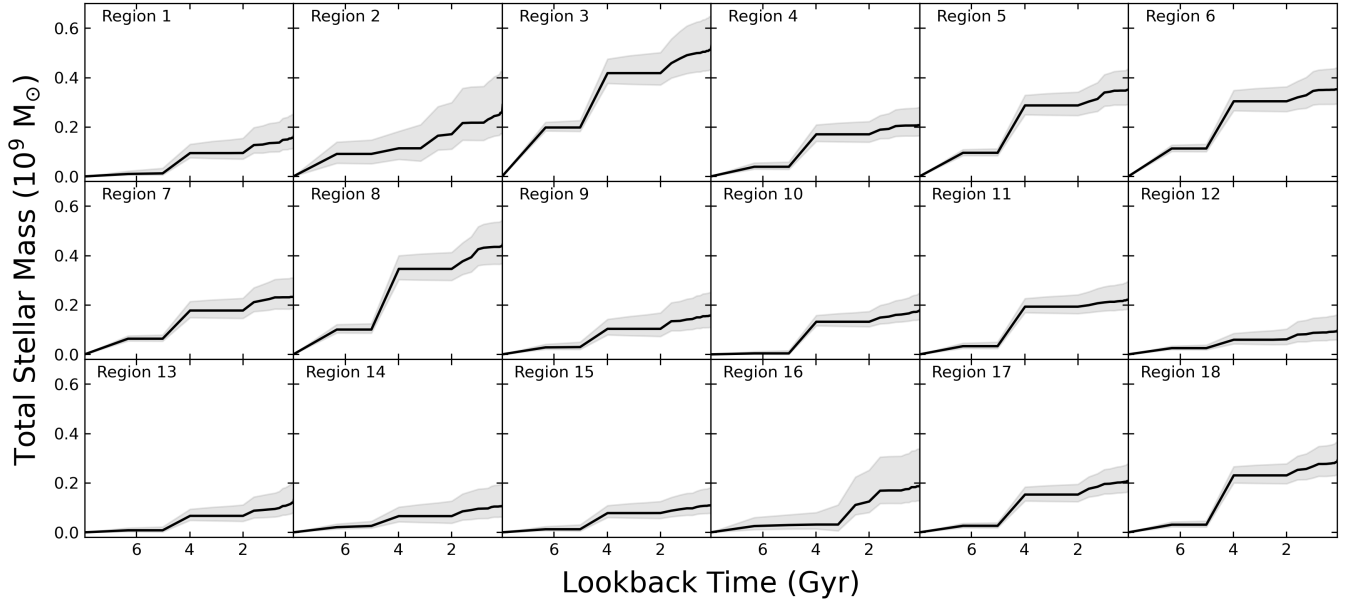


Figure 12. Cumulative stellar mass formed for the past 8 Gyr in the 18 regions, which are labeled in Figure 9.

The interaction history of NGC 205 and M31 is not as well-studied as others in the M31 system, such as M32. There is a putative tidal ‘arc’ of NGC 205 that extends to the north (regions 3, 10, 13; [McConnachie et al. 2004](#)), though its association with NGC 205 is not definitive (e.g., [Howley et al. 2008](#); [Liu et al. 2024](#)). The SFHs of NGC 205 and the arc regions appear to be anti-correlated. The similarity of SFHs between NGC 205 (region 3) and region 8, may suggest an association be-

tween the two (e.g., region 8 could be material stripped from NGC 205), but the lack of obvious tidal features in that direction from ground-based data (e.g., in the PANDAS stellar maps, [Richardson et al. 2011](#); [McConnachie et al. 2018](#)) does not support this suggestion. An interesting future angle would be to combine wide-area kinematics, such as measured from recent work with DESI ([Dey et al. 2023](#)), and potentially Subaru/PFS in the future, with the AGB-star based SFHs to see if

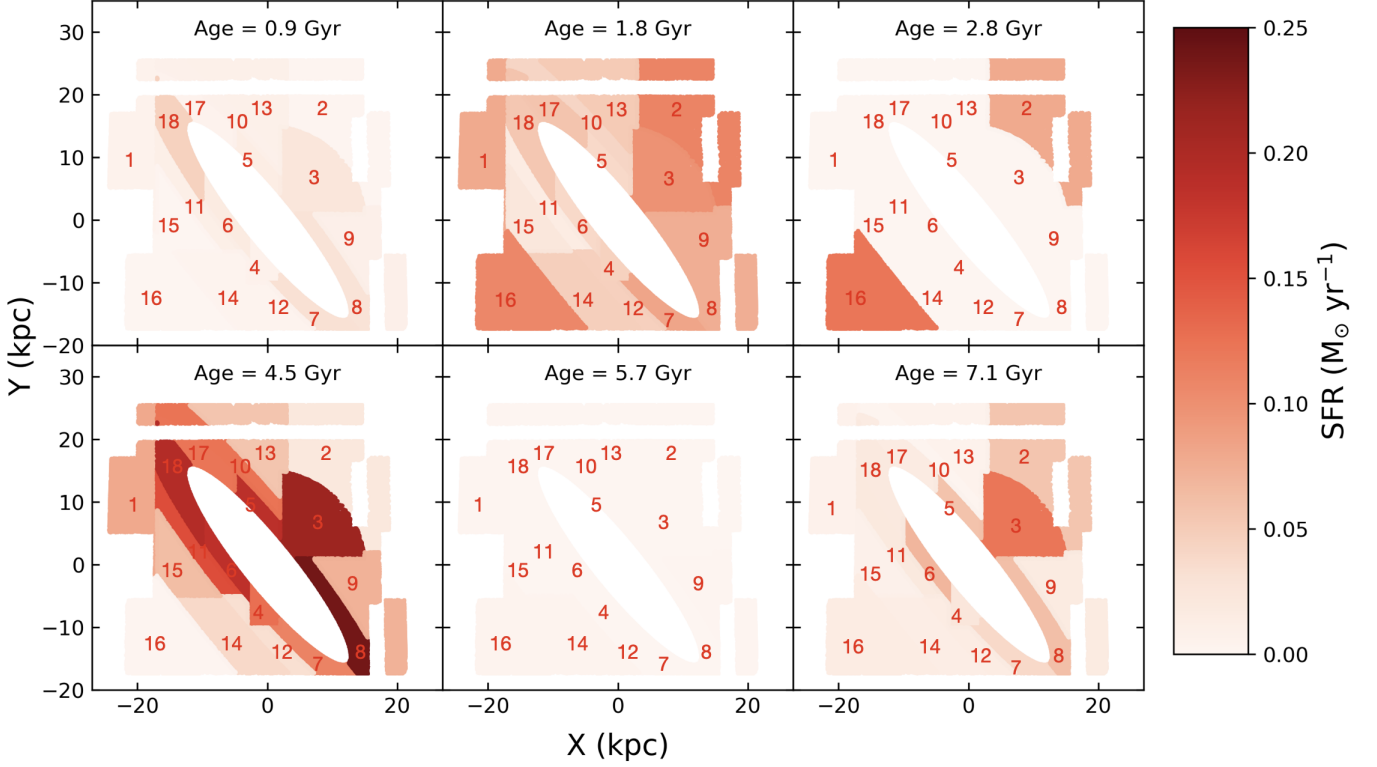


Figure 13. Star formation rate as a function of position for six different epochs.

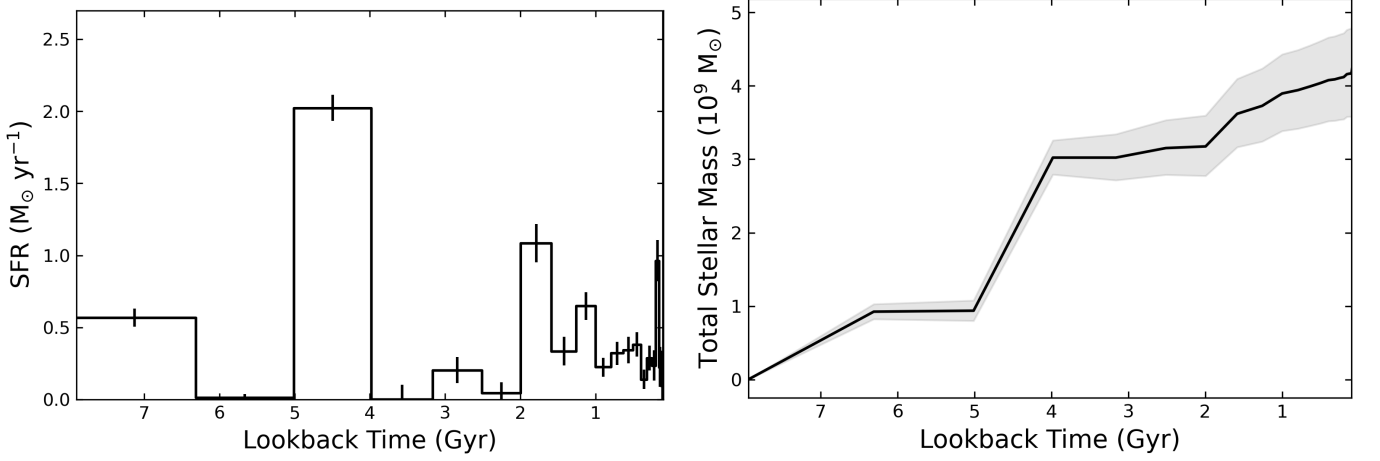


Figure 14. (Left) total star formation rate vs. age for the entire halo footprint. (Right) The cumulative stellar mass formed as a function of time.

there are clear relationships between ages and kinematics, analogous to the disk heating study of [Dorman et al. \(2015\)](#). Finally, NGC 205 currently has no published proper motions. An orbital history, in tandem with our SFHs, would be useful in helping to decipher the interaction history between NGC 205 and M31.

Another prominent sub-structure in the vicinity of M31 is M32, which is located in region 4. Our SFH of region shows a prominent burst from $\sim 4 - 5$ Gyr ago and lower levels from $\sim 1 - 3$ Gyr ago. This is qualitatively similar to the SFH measured from moderately deep HST/ACS imaging ([Savino et al. in prep.](#)).

Monachesi et al. (2012)’s SFHs from two HST/ACS HRC fields that reach the oldest MSTO in M32 show broadly similar trends, however their coarse time resolution (i.e., 2-5 Gyr, 5-12 Gyr bins) make direct comparison challenging. Several regions adjacent to M32 (regions 6, 7, 11, 15) also show enhanced star formation $\sim 4 - 5$ Gyr, which is in line with some suggestions of when M32 (or its progenitor) may have started to interact with M31. The literature is rich with plausible interaction scenarios between M32 and M31 (e.g., Cepa & Beckman 1988; Bekki et al. 2001; Choi et al. 2002; Ibata et al. 2004; Block et al. 2006; Gordon et al. 2006; Dierickx et al. 2014; D’Souza & Bell 2018). Further comparisons with predictions from detailed simulations and our SFHs may help support or rule out some of these possibilities. A detailed exploration of these scenarios is beyond the intended scope of this paper. As with NGC 205, a proper motion and orbital history of M32 is likely to greatly help interpretation.

Figure 15 shows the ‘quenching’ time in each region. As a proxy for ‘quenching’ we use the lookback time at which 90% of the stellar mass formed in each region’s cumulative SFH. Regions with larger values of t_{90} stopped forming stars before regions with smaller values of t_{90} .

In Figure 15, M32 and adjacent regions 4, 6, 7, and 11 show similar values of $t_{90} \sim 1.6$ Gyr ago, which may suggest related stellar populations. Similarly, NGC 205 and adjacent regions 5, 8, and 17 all have similar values of $t_{90} \sim 1.1$ Gyr ago. Regions 1 and 2, which contain the Eastern and Western shelves, respectively, have among the youngest stellar populations in the entire inner halo with $t_{90} \lesssim 0.5$ Gyr ago. Finally, region 16, which is in the direction of the GSS is slightly younger, $t_{90} \lesssim 0.8$ Gyr, than regions containing shelves.

On aggregate, this map indicates that star formation shut down closer to the disk of M31 ~ 1 Gyr prior to slightly more distant regions. However, the limitations of our spatial coverage, i.e., no extended and/or smooth stellar halo, make it challenging to interpret this result in a broader context. For example, the M31-M32 interaction scenario proposed by D’Souza & Bell (2018) indicates that the youngest stars should be more centrally concentrated than older stars. However, they considered a much larger spatial area overall, and a more targeted comparison is needed to see if our data are truly in tension with this scenario.

6. CAVEATS & LIMITATIONS

Despite demonstrating the power of resolved AGB stars in the NIR for SFH measurements, we emphasize a few areas of caution and items that need improvement.

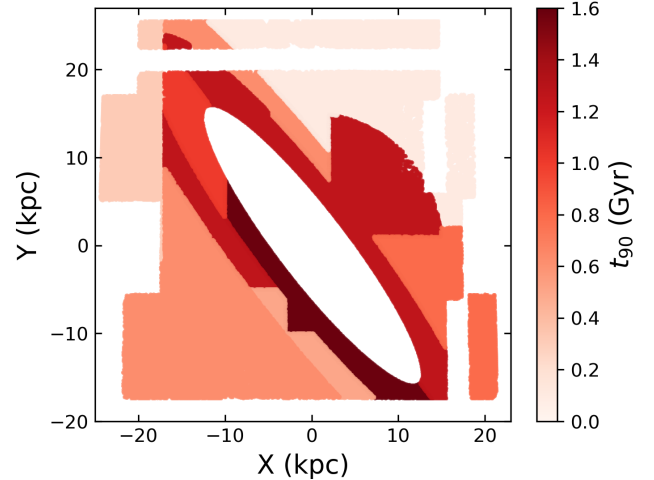


Figure 15. Time at which 90% of the stellar mass formed in each region of the inner stellar halo.

First, in this paper, we only examined AGB star-based SFHs back to ~ 8 Gyr ago. This oldest age restriction was motivated by the conservative choice to empirically vet our data against another SFH. However, in principle, as discussed in §2, it is possible to measure an AGB star-based SFH back to the oldest epoch of star formation (i.e., ~ 14 Gyr ago). While these ancient stars are unlikely to be found in the TP-AGB phase, they will appear as E-AGB stars on a NIR CMD. Indeed, ancient MW GC (e.g., NGC 6752; Norris et al. 1981) do have confirmed AGB stars, providing affirmation of this possibility. The limiting factor for testing this possibility is the lack of a suitable dataset (i.e., it must include the ancient MSTO and a suitable number of AGB stars). We plan to continue this investigation in future papers.

Second, as illustrated in Appendix A, a robust SFH requires several hundred AGB stars. Though our tests show that it is possible to recover a reliable SFH from as few as ~ 300 AGB stars, we adopt a more conservative recommendations of $\gtrsim 700$ AGB, as a means of guarding against different types of SFHs, lower quality of data, etc. that are not considered in the present analysis.

This minimum number is comfortably met by systems into the dwarf galaxy regime. For example, the SMC ($M_V = -16.8$) and NGC 6822 ($M_V = -15.2$; McConnachie 2012) each contain > 4000 AGB stars (e.g., Cioni & Habing 2005; Boyer et al. 2011), while other fainter systems have several hundred AGB stars as well (e.g., Dalcanton et al. 2012a; Boyer et al. 2015). While galaxy luminosity provides a good rule of thumb for how many AGB stars to expect, SFH is clearly an important component. Systems that are purely ancient will have fewer AGB than those with more recent star formation (i.e., within the last several Gyr). Even fairly luminous

systems with ‘pauses’ in the SFHs at intermediate ages (e.g., WLM; Albers et al. 2019; McQuinn et al. 2024a) may have fewer AGB stars than their luminosities would suggest.

Third, our AGB star-only SFHs have no systematic uncertainties. Dolphin (2012) presents a means to estimate uncertainties on SFHs measured from resolved star CMDs that are designed to capture variations in the SFHs due to choice in stellar models. The method for computing these systematics relies on being able to measure SFHs on test datasets using different stellar models. Because COLIBRI uniquely provide suitable AGB star models, it is not possible to compute analogous systematic uncertainties for our AGB star-only SFHs. Even within the COLIBRI models, specific choices are made that can affect the age characteristics of the AGB stars. For example, our basis models for this analysis were generated with a Reimers mass loss value of $\eta = 0.2$ for RGB stars. Large changes to this value can affect the evolution of AGB stars. For example, a much higher mass-loss rate on the RGB does not produce AGB stars at the oldest ages. It is not clear that such large mass-loss rates on the RGB are supported by data, but we nevertheless note this possibility. This type of choice is not unique to AGB star models. For example, the modeling of metal-diffusion in lower-mass stars can affect the lifetimes of MSTO stars, which can lead to systematically younger or older ages (e.g., Hidalgo et al. 2018).

Finally, we note that only NIR data is suitable for AGB star-only SFHs. In the optical, there is too much overlap between the RGB and AGB to provide robust SFHs. In limited exploration, this appears to be true even for a single optical (e.g., F814W or F090W) and NIR band. We have not conducted an exhaustive exploration of all possible filter combinations, but our findings thus far strongly suggest this approach is optimal with two NIR filters. Age sensitivity is improved when both sides of the typical AGB SED peak are comfortably sampled (e.g., one band at $< 1.5\mu\text{m}$ and another at $> 2\mu\text{m}$).

7. FUTURE PROSPECTS

The method we have presented is well-suited for JWST. JWST’s exquisite sensitivity in the near- and mid-IR and high angular resolution have the potential to resolve AGB stars out to tens of Mpc.

The type of JWST dataset needed to measure AGB-star SFHs is well-matched to the JAGB (e.g., Lee et al. 2024; Li et al. 2024), and to some extent, TRGB distance programs (e.g., Anand et al. 2024a,b; Hoyt et al. 2024; Newman et al. 2024). The JAGB method requires at least a few hundred AGB stars in the J region of

the NIR CMD and it often measured in filter combinations that sample either side for the SED peak of AGB stars. The high luminosity of AGB stars coupled with the characteristics of JWST suggest that AGB-based SFHs and JAGB distances already work out to 20 Mpc (e.g., Anand et al. 2024a,b; Hoyt et al. 2024; Lee et al. 2024) using $\sim 1-3$ hours of integration time. It seems clear that JAGB distances and our SFH method can be extended to galaxies out to many tens of Mpc with suitably well-planned observations (e.g., to avoid too much crowding).

Programs that aim to measure TRGB distances with JWST may also be suitable for AGB-based SFHs. The $F090W - F150W$ filter combination provides for precise TRGBs, but is not particularly good for clearly separating all AGB and RGB stars in CMD space (see e.g., various $F090W - F150W$ CMDs in Anand et al. 2024a,b; Newman et al. 2024). However, the $F115W - F277W$ filter combination appears to enable precise ($\lesssim 1.5\%$) TRGB distances (Newman et al. 2024) and appears to be a good filter combination of AGB star-based SFHs as AGB stars are both brighter in these bands, have little overlap with the RGB, and sample both sides of the SEDs peak for most AGB stars. We illustrate this further in Appendix C.

Roman and Euclid offer similar potentials for AGB star-based SFHs, though their filter ranges are a little more limited than JWST. We have not explored the specific capabilities of these facilities, but based on the $J - K$ analysis in this paper, AGB star SFHs from their NIR CMDs appear promising as well.

Beyond observational prospects, we also anticipate improvements in AGB star models. For example, improvements to the COLIBRI AGB stellar models are underway, as the COLIBRI team is actively calibrating its models in M31 and low-metallicity Local Group dwarf galaxies (Pastorelli et al. 2020).

However, robust determinations of SFHs derived from AGB stars will require investigations into the full systematic uncertainties of the fits, similar to what has been done for SFHs based on optical CMDs (e.g., Weisz et al. 2011; Dolphin 2012). As discussed in §6, we highly advocate for the development of an independent set of very detailed TP-AGB models. In addition to aiding AGB SFH studies like this one and others described in §1, another set of AGB models would improve our knowledge of the contribution of AGB stars to the integrated SEDs of galaxies at all cosmic epochs (e.g., Melbourne et al. 2012) and help with the calibration of the AGB star extragalactic distance scale, which use the P-L relations of Mira variable stars (e.g., Huang et al. 2020, 2024) or the mean luminosities of carbon stars (JAGB method; e.g.,

Madore & Freedman 2020; Ripoche et al. 2020; Zgirski et al. 2021; Lee et al. 2024).

8. CONCLUSIONS

In this work we demonstrated a new approach to measuring quantitative SFHs of galaxies using NIR observations of AGB stars, COLIBRI stellar libraries, and the MATCH CMD modeling package. Our main takeaways from this paper are:

- The potential of resolved AGB stars for measuring SFHs has long been known. Theoretical models, specifically COLIBRI, now include many detailed physical processes lacking from other models, and have been anchored by NIR observations of resolved stellar populations in the Local Group.
- The COLIBRI models show that AGB stars are highly sensitive to age and only moderately sensitive to metallicity. Ages of AGB stars range from ~ 0.1 to ~ 13 Gyr. We show that there is only a modest degeneracy between age and metallicity for AGB stars in the NIR.
- There are several advantages to measuring SFHs from resolved AGB stars in the NIR. First, AGB stars are much brighter ($M_J \lesssim -5$) than optical age sensitive features (e.g., red clump, MSTO). AGB stars in the NIR are also less impacted by dust. In the NIR AGB stars occupy a distinct region of the CMD with little-to-no overlap with other populations (e.g., RGB stars, MW foreground). In the optical, AGB stars are challenging to separate from other phases of evolution that are not age sensitive (e.g., the RGB) compromising their utility for SFH work.
- Using synthetic data, we show that arbitrary SFHs can be recovered with the widely-used CMD fitting package MATCH using only AGB stars on a NIR CMD.
- We use only AGB stars from ground-based UKIRT NIR photometry to measure the SFH over the past 8 Gyr of M31's outer disk covered by PHAT. We find our SFH to be in excellent agreement with the area-matched PHAT SFH from W17, which was derived from an optical HST-based CMD. The lookback time of this comparison is set by the fidelity of the PHAT SFH; the AGB star CMDs shows populations that are older than 8 Gyr. Our tests show that AGB stars-based SFHs can be recovered to ages older than 8 Gyr ago.
- The high luminosities of AGB stars in the NIR and their relative rarity mean that crowding effects are minimal, even across the entirety of M31's disk using UKIRT imaging (i.e., a modest-sized ground-based facility).
- By sub-sampling the number of AGB stars used for comparison against the PHAT SFH, we show that even a few hundred AGB stars can provide a robust SFH recovery. We attribute this to the strong age-sensitivity of AGB stars in the NIR.
- As a practical illustration of our AGB star SFH methodology, we measure the spatially resolved SFH of M31's inner stellar halo ($D_{\text{M31,projected}} \sim 20 - 30$ kpc. We find a nearly global burst of star formation $\sim 4 - 5$ Gyr ago and much lower level, spatially distributed star formation from $\lesssim 2$ Gyr ago. Regions associated with NGC 205 and M32 appear to be the most active. We find a total of $M_\star \sim 4 \times 10^9 M_\odot$ formed in M31's inner stellar halo in the last 8 Gyr.
- We use synthetic data to show that (a) SFHs only using NIR observations of AGB stars can robustly be recovered to lookback times of 13 Gyr ago and (b) JWST CMDs of AGB stars (e.g., $F115W - F277W$) can be used to recovery SFH across all cosmic time with similar fidelity.
- We discuss several caveats in our analysis such as the need for NIR imaging and the lack of alternative AGB star models needed to estimate systematic uncertainties on the SFHs. We provide guidance for what types of galaxies are suitable for application of this method.
- We discuss the enormous scientific potential for measuring SFHs in galaxies out to tens of Mpc using NIR observations of resolved AGB stars with JWST, Roman, and Euclid.

We sincerely thank Léo Girardi, Paola Marigo, Giada Pastorelli, and the Padova group for their extraordinary work developing the COLIBRI models which made this work possible, and for answering our questions about the stellar isochrones. A.J.L. acknowledges Meredith Durbin for useful discussions and for making their code on Hess diagrams publicly available, which we used to generate the CMDs in this paper. A.J.L. also thanks Wendy Freedman, Alex Ji, Barry Madore, and Kyle Rocha for stimulating discussions that helped inspire this work. D.R.W. thanks the Minnesota Institute for Astrophysics for hosting his sabbatical visit during the writing of this paper. A.J.L. and D.R.W. thank Quixotic Coffee in St. Paul, MN for providing a stimulating and convenient working environment.

A.J.L. was supported by the Future Investigators in NASA Earth and Space Science and Technology (FINESST) award number 80NSSC22K1602 during the completion of this work. A.J.L. thanks the LSSTC Data Science Fellowship Program, which is funded by LSSTC, NSF Cybertraining Grant #1829740, the Brinson Foundation, and the Moore Foundation; her participation in the program has benefited this work. Y.R. was supported by the National Natural Science Foundation of China (NSFC) through grant numbers 12133002 and 12203025.

This research has made use of NASA’s Astrophysics Data System Bibliographic Services. This research has made use of the NASA/IPAC infrared Science Archive (IRSA), which is operated by the Jet Propulsion Laboratory, California Institute of Technology, under contract with the National Aeronautics and Space Administration. This paper uses data from UKIRT, which is owned by the University of Hawaii (UH) and operated by the UH Institute for Astronomy

Facilities: UKIRT (WFCam)

Software: Astropy (Astropy Collaboration et al. 2013, 2018, 2022), *imf* (<https://github.com/keflavich/imf>), *MATCH* (Dolphin 2002, 2012, 2013), Matplotlib (Hunter 2007), NumPy (Harris et al. 2020), Pandas (McKinney 2010), Scikit-learn (Pedregosa et al. 2011)

APPENDIX

A. HOW MANY STARS ARE NEEDED FOR AN ACCURATE AGB SFH MEASUREMENT?

In this section, we investigate the effect of decreased sample size on the precision and accuracy of our AGB SFH measurements. As described in §5.2.2, a sample of 23,000 AGB stars delivered small statistical uncertainties that agree well systematically with the measurement from W17. To test how the uncertainties and bias change as a function of sample size, first we randomly sample 11500 AGB stars, or about 1/2 of our main sample, and re-measure the AGB SFH. We repeat this test eight more times until our sample size decreases

to ~ 300 AGB stars. In Figure A1, we show three representative fits measured from random samples of 5900 AGB stars, 760 AGB stars, and 280 AGB stars.

As expected, the statistical uncertainties increase with decreased sample size. We note a sample of 700 AGB stars deliver an AGB SFH closely matching (albeit with larger statistical errors) the AGB SFH measured from the full sample. For a sample of 300 AGB stars, the measured AGB SFH begins to systematically deviate slightly from the AGB measured from 23,000 AGB stars, particularly at older ages. Therefore, we conclude that accurate AGB SFH measurements should be based on samples of at least ~ 700 AGB stars.

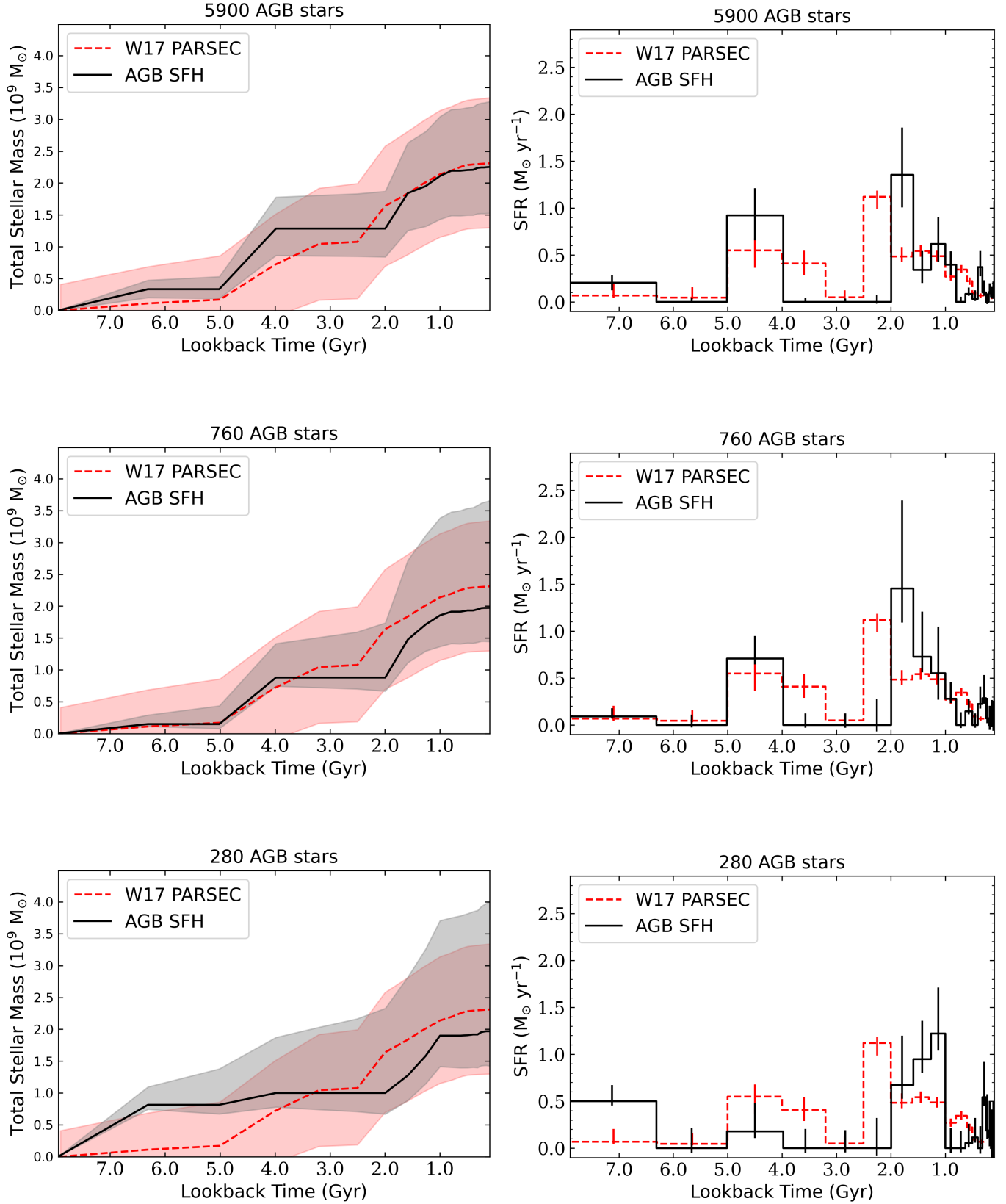


Figure A1. Accuracy and precision of AGB SFH and SFR fits as a function of the number of randomly sampled AGB stars from the full sample of $\sim 23,000$ AGB stars used in Figure 7.

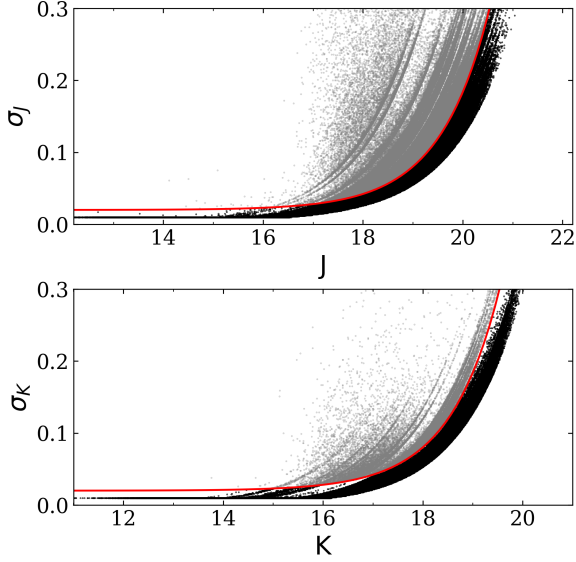


Figure B1. Photometric uncertainty as a function of J- and K-band magnitudes. Quality cuts are shown in red, with the sources passing the given restriction in black and the sources not passing the restriction in grey.

B. PHOTOMETRIC QUALITY-METRIC CUTS

We clean the UKIRT photometry used in the main text via the photometric uncertainty as a function of their J-band and K-band magnitudes. These cuts were also used in Lee (2023) who used this same photometric catalog to measure the distance to M31 with AGB stars. The functional forms of these functions are shown below and also plotted in Figure B1:

$$\sigma_J < 0.02 + 0.003 \times e^{m_J - 16} \quad (\text{B1})$$

$$\sigma_K < 0.02 + 0.003 \times e^{m_K - 15}. \quad (\text{B2})$$

C. RECOVERY OF OLDEST AGB STARS

Throughout the paper, we limit our simulated and real SFHs to a lookback time of ~ 8 Gyr ago. This age was motivated by limitations of the SFHs presented by PHAT. As discussed in W17, they only model one age bin between 8 and 14 Gyr ago, owing to the modest depth of their data. The utility of this age bin is limited for SFH validation as it essentially provides a total mass and nothing else. We found it far more valuable to focus on both comparing the normalization and timing of star formation between the our NIR AGB star approach and the SFHs from PHAT optical CMDs. When we find a suitable dataset, i.e., that has enough AGB stars and an optical CMD that reaches fainter than the oldest MSTO,

we will undertake a similar SFH comparison to older ages.

In the meantime, we use simulated data to show that, in principle, AGB star-based SFHs can be recovered back to the oldest epochs of star formation. The set up of the mock tests are the same as described in §5.1. The results for a constant SFH in the $J - K$ filter combination are shown in Figure C1. The mock tests show excellent recovery of the input SFH.

In Figure C2, we undertake the same test only using an example JWST filter set $F115W - F277W$. The motivation for this filter combination is that it is particularly efficient for measuring precise TRGB distances with JWST (e.g., Newman et al. 2024). Such data would also well-suited for measuring AGB star-based SFHs. As with the other simulated data experiments, the recovered SFH is in good agreement with the input SFH. Deviations in the SFR at early time are not statistically significant and are similar to fluctuations in CMD-based SFH recovery discussed in Dolphin (2002), and further emphasize the importance of robust statistical uncertainties (e.g., Dolphin 2013). Our purpose was largely to demonstrate the utility of excellent JWST TRGB data for this additional use case. We plan a more exhaustive exploration of JWST (as well as Roman and Euclid) filter combinations in a future paper.

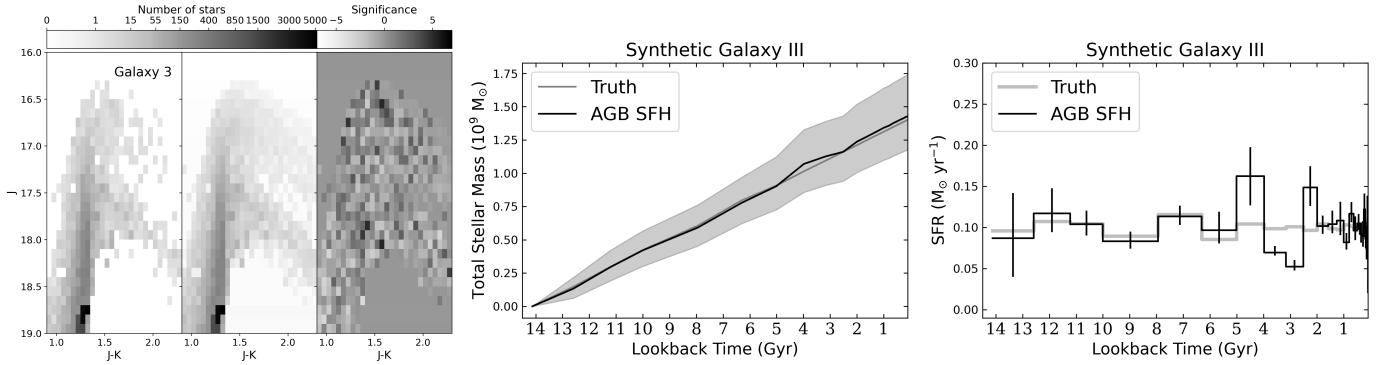


Figure C1. An example of recovering a SFH back to the oldest epochs of star formation, $\gtrsim 13$ Gyr ago, using only AGB stars in the NIR. (Left) Density maps for the observed, best-fit, and residual CMDs, expressed in units of Poisson standard deviations. (Middle) Cumulative stellar mass formed as a function of time. (Right) Total star formation rate as a function of time. The excellent agreement indicates that resolved AGB stars in the NIR, in principle, can be used to measure SFHs across all cosmic time.

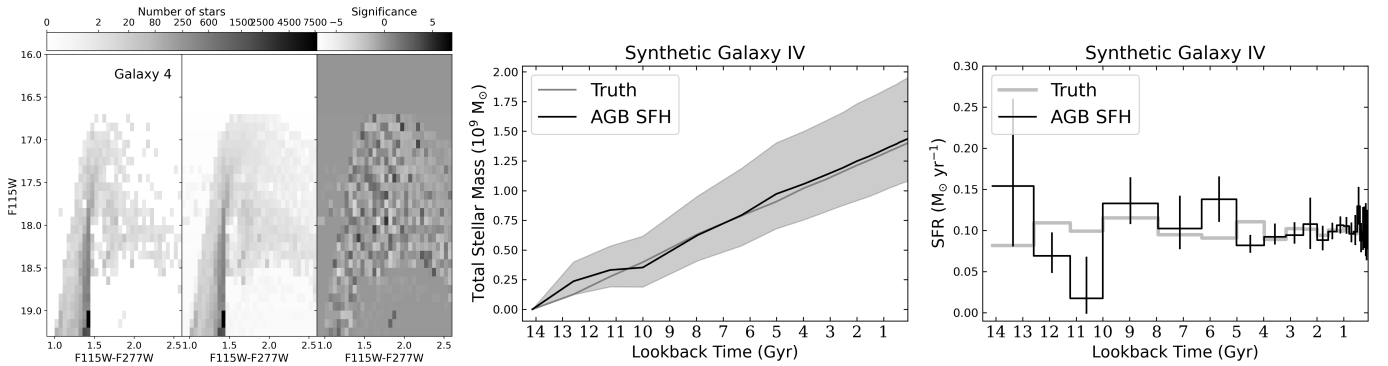


Figure C2. Same as the previous figure and test, only for the JWST filter combination $F115W-F277W$, which is recommended for precision TRGB distances (e.g., Newman et al. 2024).

REFERENCES

- Albers, S. M., Weisz, D. R., Cole, A. A., et al. 2019, *MNRAS*, 490, 5538
- Anand, G. S., Tully, R. B., Cohen, Y., et al. 2024a, *ApJ*, 973, 83
- Anand, G. S., Tully, R. B., Cohen, Y., et al. 2024b, *arXiv:2408.16810*
- Astropy Collaboration, Price-Whelan, A. M., Lim, P. L., et al. 2022, *ApJ*, 935, 167
- Astropy Collaboration, Price-Whelan, A. M., Sipőcz, B. M., et al. 2018, *AJ*, 156, 123
- Astropy Collaboration, Robitaille, T. P., Tollerud, E. J., et al. 2013, *A&A*, 558, A33
- Barmby, P., Ashby, M. L. N., Bianchi, L., et al. 2006, *ApJL*, 650, L45
- Bekki, K., Couch, W. J., Drinkwater, M. J., et al. 2001, *ApJL*, 557, L39
- Bernard, E. J., Ferguson, A. M. N., Chapman, S. C., et al. 2015a, *MNRAS*, 453, L113
- Bernard, E. J., Ferguson, A. M. N., Richardson, J. C., et al. 2015b, *MNRAS*, 446, 2789
- Bhardwaj, A., Kanbur, S. M., Macri, L. M., et al. 2016, *AJ*, 151, 88
- Block, D. L., Bornaud, F., Combes, F., et al. 2006, *Nature*, 443, 832
- Boyer, M. L., Srinivasan, S., van Loon, J. T., et al. 2011, *AJ*, 142, 103
- Boyer, M. L., McQuinn, K. B. W., Barmby, P., et al. 2015, *ApJS*, 216, 10
- Boyer, M. L., Pastorelli, G., Girardi, L., et al. 2024, *ApJ*, 973, 120
- Bressan, A., Marigo, P., Girardi, L., et al. 2012, *MNRAS*, 427, 127
- Brown, T. M., Smith, E., Ferguson, H. C., et al. 2006, *ApJ*, 652, 323
- Cardelli, J. A., Clayton, G. C., & Mathis, J. S. 1989, *ApJ*, 345, 245
- Cepa, J. & Beckman, J. E. 1988, *A&A*, 200, 21
- Chen, Y., Bressan, A., Girardi, L., et al. 2015, *MNRAS*, 452, 1068
- Chen, Y., Girardi, L., Bressan, A., et al. 2014, *MNRAS*, 444, 2525
- Choi, P. I., Guhathakurta, P., & Johnston, K. V. 2002, *AJ*, 124, 310
- Cioni, M.-R. L. & Habing, H. J. 2005, *A&A*, 429, 837
- Cioni, M.-R. L., Girardi, L., Marigo, P., et al. 2006, *A&A*, 448, 77
- Cioni, M.-R. L., Irwin, M., Ferguson, A. M. N., et al. 2008, *A&A*, 487, 131
- Cole, A. A., Weisz, D. R., Dolphin, A. E., et al. 2014, *ApJ*, 795, 54
- Costa, E. & Frogel, J. A. 1996, *AJ*, 112, 2607
- Crnojević, D., Ferguson, A. M. N., Irwin, M. J., et al. 2013, *MNRAS*, 432, 832
- Dalcanton, J. J., Williams, B. F., Melbourne, J. L., et al. 2012a, *ApJS*, 198, 6
- Dalcanton, J. J., Williams, B. F., Lang, D., et al. 2012b, *ApJS*, 200, 18
- Dalcanton, J. J., Fouesneau, M., Hogg, D. W., et al. 2015, *ApJ*, 814, 3
- Davidge, T. J. 2003, *ApJ*, 597, 289.
- Davidge, T. J. 2005, *AJ*, 130, 2087
- Davidge, T. J. 2014, *ApJ*, 791, 66
- de Boer, T. J. L., Tolstoy, E., Hill, V., et al. 2012a, *A&A*, 539, A103
- de Boer, T. J. L., Tolstoy, E., Hill, V., et al. 2012b, *A&A*, 544, A73
- de Boer, T. J. L., Tolstoy, E., Lemasle, B., et al. 2014, *A&A*, 572, A10
- de Boer, T. J. L., Tolstoy, E., Saha, A., et al. 2011, *A&A*, 528, A119
- de Grijs, R. & Bono, G. 2014, *AJ*, 148, 17
- Dey, A., Najita, J. R., Koposov, S. E., et al. 2023, *ApJ*, 944, 1
- Dierickx, M., Blecha, L., & Loeb, A. 2014, *ApJL*, 788, L38
- Dolphin, A. E. 2002, *MNRAS*, 332, 91
- Dolphin, A. E. 2012, *ApJ*, 751, 60
- Dolphin, A. E. 2013, *ApJ*, 775, 76
- Dolphin, A. E., Saha, A., Skillman, E. D., et al. 2003, *AJ*, 126, 187
- Dorman, C. E., Guhathakurta, P., Seth, A. C., et al. 2015, *ApJ*, 803, 24
- Draine, B. T., Aniano, G., Krause, O., et al. 2014, *ApJ*, 780, 172
- D’Souza, R. & Bell, E. F. 2018, *Nature Astronomy*, 2, 737
- Fardal, M. A., Babul, A., Guhathakurta, P., et al. 2008, *ApJL*, 682, L33
- Fardal, M. A., Babul, A., Geethan, J. J., et al. 2006, *MNRAS*, 366, 1012
- Fardal, M. A., Guhathakurta, P., Gilbert, K. M., et al. 2012, *MNRAS*, 423, 3134
- Ferguson, A. M. N., Irwin, M. J., Ibata, R. A., et al. 2002, *AJ*, 124, 1452
- Ferguson, A. M. N., Johnson, R. A., Faria, D. C., et al. 2005, *ApJL*, 622, L109
- Frogel, J. A. & Blanco, V. M. 1983, *ApJL*, 274, L57
- Gallart, C., Aparicio, A., Bertelli, G., et al. 1996, *AJ*, 112, 1950

- Gallart, C., Zoccali, M., & Aparicio, A. 2005, *ARA&A*, 43, 387
- Geha, M., Weisz, D., Grocholski, A., et al. 2015, *ApJ*, 811, 114
- Gordon, K. D., Bailin, J., Engelbracht, C. W., et al. 2006, *ApJL*, 638, L87
- Gegersen, D., Seth, A. C., Williams, B. F., et al. 2015, *AJ*, 150, 189
- Habing, H. J. & Olofsson, H. 2003, *Asymptotic Giant Branch stars* (New York: Springer)
- Hamedani Golshan, R., Javadi, A., van Loon, J. T., et al. 2017, *MNRAS*, 466, 1764
- Hamren, K. M., Rockosi, C. M., Guhathakurta, P., et al. 2015, *ApJ*, 810, 60
- Harmsen, B., Bell, E. F., D’Souza, R., et al. 2023, *MNRAS*, 525, 4497
- Harris, C. R., Millman, K. J., van der Walt, S. J., et al. 2020, *Nature*, 585, 357
- Hidalgo, S. L., Aparicio, A., Skillman, E., et al. 2011, *ApJ*, 730, 14
- Hidalgo, S. L., Pietrinferni, A., Cassisi, S., et al. 2018, *ApJ*, 856, 125
- Howley, K. M., Geha, M., Guhathakurta, P., et al. 2008, *ApJ*, 683, 722
- Hodgkin, S. T., Irwin, M. J., Hewett, P. C., et al. 2009, *MNRAS*, 394, 675
- Hoyt, T. J., Jang, I. S., Freedman, W. L., et al. 2024, *arXiv:2407.07309*
- Huang, C. D., Riess, A. G., Yuan, W., et al. 2020, *ApJ*, 889, 5
- Huang, C. D., Yuan, W., Riess, A. G., et al. 2024, *ApJ*, 963, 83
- Hunt, L. K., Annibali, F., Cuillandre, J.-C., et al. 2024, *arXiv:2405.13499*
- Hunter, J. D. 2007, *Computing in Science and Engineering*, 9, 90
- Ibata, R., Chapman, S., Ferguson, A. M. N., et al. 2004, *MNRAS*, 351, 117
- Iben, I. & Renzini, A. 1983, *ARA&A*, 21, 271
- Irwin, M. J., Lewis, J., Hodgkin, S., et al. 2004, *Proc. SPIE*, 5493, 41
- Javadi, A., van Loon, J. T., & Mirtorabi, M. T. 2011, *MNRAS*, 414, 3394
- Jeffery, E. J., Smith, E., Brown, T. M., et al. 2011, *AJ*, 141, 171
- Jung, M. Y., Ko, J., Kim, J.-W., et al. 2012, *A&A*, 543, A35
- Lazzarini, M., Williams, B. F., Durbin, M. J., et al. 2022, *ApJ*, 934, 76
- Lee, M. G. 1996, *AJ*, 112, 1438
- Lee, A. J., Freedman, W. L., Madore, B. F., et al. 2021, *ApJ*, 907, 112
- Lee, A. J. 2023, *ApJ*, 956, 15
- Lee, A. J., Freedman, W. L., Madore, B. F., et al. 2024, *arXiv:2408.03474*
- Li, S., Riess, A. G., Casertano, S., et al. 2024, *ApJ*, 966, 20
- Liu, Z., Wang, J., Jing, Y., et al. 2024, *Research in Astronomy and Astrophysics*, 24, 085005
- Lewis, A. R., Dolphin, A. E., Dalcanton, J. J., et al. 2015, *ApJ*, 805, 183
- Kroupa, P. 2001, *MNRAS*, 322, 231
- Madore, B. F. & Freedman, W. L. 2020, *ApJ*, 899, 66
- Maraston, C., Daddi, E., Renzini, A., et al. 2006, *ApJ*, 652, 85
- Marigo, P., Bressan, A., Nanni, A., et al. 2013, *MNRAS*, 434, 488
- Marigo, P. & Girardi, L. 2007, *A&A*, 469, 239
- Marigo, P., Girardi, L., Bressan, A., et al. 2008, *A&A*, 482, 883
- Marigo, P., Girardi, L., Bressan, A., et al. 2017, *ApJ*, 835, 77
- McConnachie, A. W. 2012, *AJ*, 144, 4
- McConnachie, A. W., Irwin, M. J., Lewis, G. F., et al. 2004, *MNRAS*, 351, L94
- McConnachie, A. W., Irwin, M. J., Ferguson, A. M. N., et al. 2005, *MNRAS*, 356, 979
- McConnachie, A. W., Ibata, R., Martin, N., et al. 2018, *ApJ*, 868, 55
- McKinney, W. 2010, *Proceedings of the 9th Python in Science Conference*, 51-56
- McQuinn, K. B. W., Cannon, J. M., Dolphin, A. E., et al. 2015, *ApJ*, 802, 66
- McQuinn, K. B. W., Boyer, M. L., Mitchell, M. B., et al. 2017, *ApJ*, 834, 78
- McQuinn, K. B. W., B. Newman, M. J., Savino, A., et al. 2024a, *ApJ*, 961, 16
- McQuinn, K. B. W., Mao, Y.-Y., Tollerud, E. J., et al. 2024b, *ApJ*, 967, 161
- McQuinn, K. B. W., Newman, M. J. B., Skillman, E. D., et al. 2024, *arXiv:2409.19050*
- McQuinn, K. B. W., Skillman, E. D., Cannon, J. M., et al. 2010, *ApJ*, 721, 297
- Melbourne, J. & Boyer, M. L. 2013, *ApJ*, 764, 30
- Melbourne, J., Williams, B., Dalcanton, J., et al. 2010, *ApJ*, 712, 469
- Melbourne, J., Williams, B. F., Dalcanton, J. J., et al. 2012, *ApJ*, 748, 47
- Monachesi, A., Trager, S. C., Lauer, T. R., et al. 2012, *ApJ*, 745, 97

- Monaco, L., Saviane, I., Perina, S., et al. 2009, *A&A*, 502, L9
- Monelli, M., Hidalgo, S. L., Stetson, P. B., et al. 2010, *ApJ*, 720, 1225
- Muñoz, R. R., Côté, P., Santana, F. A., et al. 2018, *ApJ*, 860, 66
- Nally, C., Jones, O. C., Lenkić, L., et al. 2024, *MNRAS*, 531, 183
- Newman, M. J. B., McQuinn, K. B. W., Skillman, E. D., et al. 2024, *arXiv:2406.03532*
- Nieten, C., Neiningen, N., Guélin, M., et al. 2006, *A&A*, 453, 459
- Norris, J., Cottrell, P. L., Freeman, K. C., et al. 1981, *ApJ*, 244, 205
- Pastorelli, G., Marigo, P., Girardi, L., et al. 2019, *MNRAS*, 485, 5666
- Pastorelli, G., Marigo, P., Girardi, L., et al. 2020, *MNRAS*, 498, 3283
- Pedregosa, F., Varoquaux, G., Gramfort, A., et al. 2011, *Journal of Machine Learning Research*, 12, 2825
- Reid, N. & Mould, J. 1984, *ApJ*, 284, 98
- Rejkuba, M., Harris, W. E., Greggio, L., et al. 2022, *A&A*, 657, A41
- Ren, Y., Jiang, B., Yang, M., et al. 2021, *ApJ*, 907, 18
- Ren, Y., Jiang, B., Wang, Y., et al. 2024, *ApJ*, 966, 25
- Rezaeikh, S., Javadi, A., Khosroshahi, H., et al. 2014, *MNRAS*, 445, 2214
- Richardson, J. C., Ferguson, A. M. N., Johnson, R. A., et al. 2008, *AJ*, 135, 1998
- Richardson, J. C., Irwin, M. J., McConnachie, A. W., et al. 2011, *ApJ*, 732, 76
- Richer, H. B., Crabtree, D. R., & Pritchett, C. J. 1984, *ApJ*, 287, 138
- Ripoche, P., Heyl, J., Parada, J., et al. 2020, *MNRAS*, 495, 285
- Rose, J. A., Arimoto, N., Caldwell, N., et al. 2005, *AJ*, 129, 712
- Rosenfield, P., Marigo, P., Girardi, L., et al. 2014, *ApJ*, 790, 22
- Rosenfield, P., Marigo, P., Girardi, L., et al. 2016, *ApJ*, 822, 73
- Savino, A., Weisz, D. R., Skillman, E. D., et al. 2022, *ApJ*, 938, 101
- Savino, A., Weisz, D. R., Skillman, E. D., et al. 2023, *ApJ*, 956, 86
- Schlaflly, E. F. & Finkbeiner, D. P. 2011, *ApJ*, 737, 103
- Schlegel, D. J., Finkbeiner, D. P., & Davis, M. 1998, *ApJ*, 500,
- Sharina, M. E., Afanasiev, V. L., & Puzia, T. H. 2006, *MNRAS*, 372, 1259
- Skillman, E. D., Monelli, M., Weisz, D. R., et al. 2017, *ApJ*, 837, 102525
- Skillman, E. D., Tolstoy, E., Cole, A. A., et al. 2003, *ApJ*, 596, 253
- Skillman, E. D., Monelli, M., Weisz, D. R., et al. 2017, *ApJ*, 837, 102
- Skrutskie, M. F., Cutri, R. M., Stiening, R., et al. 2006, *AJ*, 131, 1163
- Tang, J., Bressan, A., Rosenfield, P., et al. 2014, *MNRAS*, 445, 4287
- Weisz, D. R., Dalcanton, J. J., Williams, B. F., et al. 2011, *ApJ*, 739, 5
- Weisz, D. R., Dolphin, A. E., Skillman, E. D., et al. 2014, *ApJ*, 789, 147
- Weisz, D. R., Savino, A., & Dolphin, A. E. 2023a, *ApJ*, 948, 50
- Weisz, D. R., McQuinn, K. B. W., Savino, A., et al. 2023b, *ApJS*, 268, 15
- Williams, B. F., Dalcanton, J. J., Seth, A. C., et al. 2009, *AJ*, 137, 41
- Williams, B. F., Dolphin, A. E., Dalcanton, J. J., et al. 2017, *ApJ*, 846, 145
- Williams, B. F., Durbin, M., Lang, D., et al. 2023, *ApJS*, 268, 48
- Williams, B. F., Lang, D., Dalcanton, J. J., et al. 2014, *ApJS*, 215, 9
- Wood, P. R., Bessell, M. S., & Paltoglou, G. 1985, *ApJ*, 290, 477
- Zgirski, B., Pietrzyński, G., Gieren, W., et al. 2021, *ApJ*, 916, 19